Review

Discovery-based design of transparent conducting oxide films

Gregory J. Exarhos *, Xiao-Dong Zhou

Pacific Northwest National Laboratory, Richland, WA 99352, USA

Abstract

The properties of TCO materials derive from the nature, number, and atomic arrangements of metal cations in crystalline or amorphous oxide structures, from the resident morphology, and from the presence of intrinsic or intentionally introduced defects. An enormous body of literature can be accessed from which empirical relationships between structure, composition, charge transport, and transparency have been developed. Previous reviews of this subject have indicated how such information may be used for engineering TCO properties; however, application of more rigorous science-based approaches to the design of materials with superior properties has only recently been tackled. This article summarizes current TCO research results, reviews processing approaches, presents a microscopic description of electronic conductivity in transparent metal oxide systems, and offers guidelines for the design and subsequent development of new materials. The review concludes with a glimpse of some recent work where impedance matching and quantum mechanical tunneling approaches would seem to provide future directions for improving transmissivity in these and similar conducting oxide systems.
© 2007 Elsevier B.V. All rights reserved.

Keywords: Transparent conducting oxide; Conductivity; Transparency; Modeling; Film deposition

Contents

---

* Corresponding author. Tel.: +1 509 376 4125; fax: +1 509 376 5106.
  E-mail address: greg.exarhos@pnl.gov (G.J. Exarhos).

1. Introduction

Transparent conducting oxides (TCO's) comprise a class of materials that can be thought of as conjugate property materials in which one property, in this case conductivity, is strongly coupled to a second property, namely, the lossy part of the refractive index or the extinction coefficient. In this regard, materials, like metals, that are highly conductive, will not normally transmit visible light, while highly transparent media like oxide glasses behave as insulators. The challenge for achieving materials that are both conducting and optically transmissive is to understand the fundamental materials structure/property relationships that drive these properties so that they may be decoupled such that the material both retains transparency while becoming electrically conductive. To an extent, many phenomenological approaches based upon well-understood physical principles have been reported to achieve materials having these properties. More recent studies push the envelope of the earlier work through understanding, at a fundamental level, the microscopic nature of the conductivity process in order to discover the role of chemical structure, bonding, and film morphology on charge transport.

The first realization of a TCO material occurred a century ago when a thin film of sputter deposited cadmium metal underwent incomplete thermal oxidation upon post-deposition heating in air [1]. While the electrical conductivity of this material did in fact change with time, the oxide was indeed representative of a free-carrier like conductor where a resident oxygen deficiency lends free carriers to associated metal defect energy levels near the bottom of the metal-like conduction band of the oxide. The generalization here is that certain slightly reduced metal oxide systems can show n-type electrical conductivity provided that charge-compensating electrons can be promoted to the conduction band of the metal oxide from defect energy levels lying close in energy to the conduction band minimum. Since this early discovery, appreciable values of electrical conductivity have been observed in many single, binary, ternary and quaternary metal oxide systems [2–7]. However, while transmission through these materials in the visible region of the spectrum can be quite good, electrical conductivities still remain considerably below those of metals.

More recently, p-type conductivity has been documented in certain metal oxide systems where the defect energy levels lie proximate to the valence band of the metal oxide [8]. In such materials, electron promotion to these defect levels creates holes in the valence band thereby promoting conductivity. Again, good transmission in the visible region of the spectrum can be achieved but measured conductivities are considerably smaller than those exhibited by the n-type materials owing to restricted hole mobility in the valence band of the solid [9].

An alternative model for describing conductivity in metal oxide systems invokes the presence of localized charge states (polarons) that transport through the lattice by means of a hopping mechanism [10]. The analogy here is to conjugated polymer systems where addition of an electron withdrawing group like iodine will abstract electrons from the extended network of carbon–carbon double bonds, forming localized charge states (holes) within the polymer chain. The motion of these trapped charge states along the chain is thermally activated and also enhanced by dynamic conformational perturbations of the polymer structure; both effects promote conductivity [10–13]. A similar mechanism can persist in metal oxide systems where strong covalent interactions between resident metal cations and oxygen prevail [14]. While visible transparency can suffer somewhat, conductivities in these metal oxide systems markedly exceed those registered by p-type free carrier oxide conductors [15]. The polaron model for describing conductivity in mixed metal oxide systems remains quite controversial.

A previous review of transparent conductors in this Journal appeared some two-dozen years ago. This earlier comprehensive article summarized work in this rapidly changing field and referenced additional review papers on this topic [2–7]. More recent advances toward our understanding of TCO properties, processing issues, and current and prospective applications have been collected in the August 2000 issue of the MRS Bulletin [16]. In the ensuing years, this topic has been featured in numerous conference symposia and workshops, most recently at the ITCO conference in Crete [17].

The review presented here summarizes recent work in this rapidly evolving area. Relationships between film processing parameters and attendant film properties are addressed along with current theoretical views on charge transport in oxide semiconductors with a goal of providing a set of unified design criteria for achieving optimum conductivity and high transmissivity. Key ideas that lead to a better understanding of charge mobility and property robustness are also discussed. Finally, future directions in which this field may grow are discussed on the basis of several recent papers dealing with impedance matching in multilayered films and quantum mechanical tunneling through a barrier.

2. Mechanisms and modeling of charge transport

The current understanding of conductivity in transparent materials is based upon a classical description of charge transport in metals coupled to the optical properties of the material through the density of charge carriers and their effective mass. A summary of the key concepts provided below defines the

relevant parameters used to describe the performance of these materials. These include the conductivity (σ), sheet resistance (R_s), free carrier mobility (μ), free carrier density (N), and the imaginary or lossy part of the refractive index termed the extinction coefficient (κ) that is proportional to the absorption coefficient (α) through the wavelength (λ).

$$I = I_0\exp(-\alpha d), \text{ with } \alpha = 4\pi\kappa/\lambda \tag{1}$$

Here, I_0 is the incident light intensity on a material of thickness d, and I is defined as the transmitted intensity through the material. Proper use of this equation for thin films requires that optical scattering and reflection losses at the interfaces be considered.

A quantitative measure of performance of a TCO can be written in terms of the ratio of the electrical conductivity to the optical absorption coefficient or,

$$\sigma/\alpha = 1[R_s\ln(T + R)]^{-1}, \tag{2}$$

where, T and R represent the total transmittance and reflectance of the material, and R_s is the sheet resistance (=resistivity/film-thickness) [18]. This figure-of-merit is used to assess the relative performance of different TCO materials and is wavelength dependent. It should be noted here that the factors appearing in Eq. (2) are highly dependent upon processing conditions and hence, the resident microstructure and defect chemistry of the material. Thus, a highly optically scattering material, due to the presence of a polycrystalline grain structure, will have both diminished transmission, and higher resistivity due to a decrease in charge mobility arising from scattering of charge carriers at grain boundaries. The figure-of-merit provides a good qualitative estimate of TCO performance for materials having similar microstructure.

The section below begins with a classical description of conductivity in condensed phases and is followed by a semi-empirical description of microscopic properties (e.g., atom size, arrangement, and coordination) of these materials that would seem to promote conductivity. Finally, key results of *ab initio* energy band structure calculations are summarized. Results from these studies can be integrated into a unified picture that can provide guidance for the development of next generation TCO materials.

2.1. Classical theory of charge transport

Consider metal as a regular 3-dimensional lattice of cations bound together by a sea of electrons that are free to move throughout the lattice. In the absence of an applied field, the motion is random. The current (I_A) in a metal segment of length L is defined to be proportional to the voltage drop (V) across that segment:

$$I_A = V/R_\Omega, \text{ or } V = I_AR_\Omega. \tag{3}$$

The resistance R_Ω is related to the length of the segment and is inversely proportional to the cross-sectional area (A).

$$R_\Omega = \rho L/A, \tag{4}$$

where ρ is the resistivity (Ω cm). For a uniform electric field (E) across L, $V=EL$ and therefore,

$$I_A = V/R_\Omega = EL/\rho L/A = EA/\rho. \tag{5}$$

Now, the current in a segment is related to the number of electrons per unit volume, $n_e=N_e/V_{vol}$, the drift velocity v_d, the magnitude of the electron charge (e) and the cross-section (A).

$$I_A = n_eeAv_d \text{ or } \rho = E/(n_eev_d). \tag{6}$$

Based upon Ohm's law, ρ must be independent of E, so therefore, the drift velocity (v_d) must be proportional to E. In the presence of an external electric field, a free electron feels a force of magnitude eE. If this were the only force, the electron of mass m_e would have an unbounded acceleration eE/m_e. However, a steady-state situation persists in which the electron drift velocity is proportional to the applied field. Therefore, collision with a lattice ion retards electron movement. After the collision, the velocity is unrelated to the drift velocity. If τ is the average time between collisions, the drift velocity of the electron becomes,

$$v_d = (eE/m_e)\tau, \tag{7}$$

and therefore,

$$\rho = E/(n_ee[eE\tau/m_e]) = m_e/(n_ee^2\tau). \tag{8}$$

This can also be written in terms of the electron mean free path, l_T, where

$$l_T = v_F\tau, \text{ and } \rho = m_ev_F/n_ee^2l_\tau. \tag{9}$$

From Ohm's law, the current density $J_e=\sigma_eE$, where J_e is the number of carriers passing through a unit area per second, and σ_e is the conductivity. Physically, σ_e^o is the *dc* current density per unit electric field, so in terms of the carrier concentration (number of electrons per unit volume),

$$J_e = N_eev_F = n_ee(e\tau/m_e)E. \tag{10}$$

(This result is obtained by counting the number of carriers, electrons of Fermi velocity $v_F(=\hbar k_F/m_e)$, that will pass through a unit area per unit time, and dividing by the field E.) The conductivity, σ_e^o, is $1/\rho$ and now becomes:

$$\sigma_e^o = n_ee^2\tau/m_e = N_ee\mu_e, \tag{11}$$

where μ_e is commonly called the carrier mobility (cm^2 V^{-1} s^{-1}). The mobility is given by:

$$\mu_e = e\tau/m_e. \tag{12}$$

This conductivity relationship is not as simplistic as it seems and in fact does contain some hidden information. The above equation was derived for a "free" electron, but in a crystalline lattice, the electron indeed is subjected to other forces that act to "alter its mass". Also, as a result of these other forces, the collision time, τ, can influence the value of m. We can therefore generalize the electron mass to account for these forces and

realize that essentially it is somewhat different from the mass of a truly free electron. As the number of electron collisions increase, the effective mass of the electron changes (m_e^*).

$$\sigma_e^o = n_e e^2 \tau / m_e^*. \tag{13}$$

The above equation relates the conductivity to the number of charge carriers and their mobility. It is understood that the mobility generalizes all the forces acting on the electron in the conducting solid. These then, are taken as the important parameters to be used for characterizing charge transport in conducting materials.

2.2. Origins of the dielectric constant — The Harmonic Oscillator

The free carriers will interact with an applied optical field through the polarization. Consider a free carrier of mass m weakly bound in a lattice by a restoring force with a force constant k_f. If the applied field oscillates at a high frequency so that the free carrier mass inertia precludes motion, there will be no coupling to the field, no loss due to absorption, and the transmission will be high. However, if the weakly bound carrier can freely respond to the field, there will be loss. A simple harmonic oscillator formalism can be used to model this interaction.

The carriers are displaced an average distance, x, from the equilibrium position resulting in an induced polarization (P).

$$P = n_e e x, \tag{14}$$

where n_e is the free carrier density, and e is the charge. The polarization electric field is P/ε, where ε is the dielectric constant of the medium. Since the force is just the charge multiplied by the field, the equation of motion for the free carrier, with a negative restoring force, can be written as,

$$m \mathrm{d}^2 x / \mathrm{d} t^2 = -n_e e^2 x / \varepsilon. \tag{15}$$

This equation of motion has an oscillatory solution,

$$x = A \exp i(n_e e^2 / m \varepsilon) t = A \exp i(\omega_p t), \tag{16}$$

where the plasma frequency, ω_p, is given by,

$$\omega_p = \{n_e e^2 / m \varepsilon\}^{1/2}. \tag{17}$$

From the conductivity relationship derived previously,

$$\omega_p^2 = \sigma_e^o / \varepsilon \tau = n_e e \mu_e / \varepsilon \tau. \tag{18}$$

The conductivity is related to the plasma frequency. Motion of the free carriers is impeded owing to collisions with the lattice and resident defects, so we must introduce a damping term into the equation of motion. These "frictional" forces are proportional to the velocity (v) and mass (m) and are inversely proportional to the time between collisions (τ). Under the influence of an oscillatory electric field,

$$m \mathrm{d} v / \mathrm{d} T + (m/\tau) v = -e E(t) = -e \exp(i \omega t), \tag{19}$$

where ω is the frequency of the applied field. A steady state solution for the velocity is:

$$v = e \tau E(t) / \{m[1 + i \omega t]\}. \tag{20}$$

Since the conductivity (σ) is defined as the current density ($J = n_e e v_F$) per unit electric field, the conductivity can be written as [19]:

$$\sigma = n_e e^2 \tau / m \{1/(1 + i \omega t)\} = \sigma_e^o \{1/(1 + i \omega t)\}, \text{ or} \tag{21}$$

$$\sigma = \sigma_e^o \{1/(1 + \omega^2 t^2)\} + i \sigma_e^o \{\omega t/(1 + \omega^2 t^2)\}. \tag{22}$$

The complex refractive index $<n>$ is written in terms of a real part (n) and a lossy part (κ) also known as the extinction coefficient.

$$<n> = n + i \kappa. \tag{23}$$

From Maxwell's equations, propagation of a wave through a solid depends upon the dielectric constant (ε) that defines the magnitude of the displacement currents due to the time variation of the applied field, and the conductivity (σ), which is a measure of the real current in the material that is created by the electric field. Therefore,

$$<n>^2 = (n + i \kappa)^2 = \varepsilon_L / \varepsilon_o - i \sigma / \omega \varepsilon_o, \tag{24}$$

where ε_L is the lattice contribution to the dielectric constant of the material (a number that represents the dielectric constant of the perfect lattice without any free carriers) and ε_o is the dielectric constant or electric permittivity of free space. Rewriting the conductivity equation in terms of the complex dielectric constant

$$\varepsilon_o = \varepsilon_o' + i \varepsilon_o'', \tag{25}$$

$$\begin{aligned} \varepsilon' &= n^2 + \kappa^2 = \varepsilon_L / \varepsilon_o - \sigma / \omega \varepsilon_o \{\omega t/(1 + \omega^2 t^2)\} \\ &= \varepsilon_L / \varepsilon_o - N_e e^2 \tau / m \omega \varepsilon_o \{\omega t/(1 + \omega^2 t^2)\}, \\ &= \varepsilon_L / \varepsilon_o - N_e e \mu / \omega \varepsilon_o \{\omega t/(1 + \omega^2 t^2)\}, \text{ and} \end{aligned} \tag{26}$$

$$\varepsilon' = \varepsilon_L / \varepsilon_o \{1 - \omega_p^2 / (\omega^2 + t^{-2})\}. \tag{27}$$

Similarily,

$$\begin{aligned} \varepsilon'' &= 2 n \kappa = \sigma / \omega \varepsilon_o \{1/(1 + \omega^2 t^2)\}, \\ &= n_e e^2 \tau / m \omega \varepsilon_o \{1/(1 + \omega^2 t^2)\}, \\ &= n_e e \mu / \omega \varepsilon_o \{1/(1 + \omega^2 t^2)\}, \text{ and} \end{aligned} \tag{28}$$

$$\varepsilon'' = \varepsilon_L / \omega \tau \varepsilon_o \{\omega_p^2 / (\omega^2 + t^{-2})\}. \tag{29}$$

The specular reflectivity (R) of a material is defined in terms of the dielectric constant:

$$R = |\varepsilon^{1/2} - 1|^2 / |\varepsilon^{1/2} + 1|^2, \tag{30}$$

or, for a non-lossy material,

$$R = (n - 1)^2 / (n + 1)^2. \tag{31}$$

These equations, then, relate the optical properties of a material to the electrical properties through the conductivity and the dielectric constant. They can be used to explore how the reflectance of a material varies with the fundamental parameters appearing in the above equations and ultimately can be used as a phenomenological guide to the design of transparent conducting films.

When this formalism is applied to a large bandgap semiconductor, the region of optical transparency becomes bounded at the high-energy side, by the strongly allowed electronic bandgap transition between the valence band maximum (VBM) and the conduction band minimum (CBM) and at the low energy side by the free carrier or plasma resonance absorption. Fig. 1 shows transmission and reflection spectra from ultraviolet to near infrared wavelengths of a conducting fluorine doped tin oxide film sputter deposited onto a borosilicate glass substrate. Loss in transmission at high and low energies is ascribed to free carrier absorption and interband electronic transitions, respectively. According to Eqs. (17) and (18), the plasma resonance frequency for free carrier conductors will increase with carrier density and decreasing free carrier mass placing a limit on the optimum region of transparency associated with a particular conductivity.

2.3. Electron energy bands in free carrier TCO's

One approach whereby electrical conductivity can be imparted to a transparent wide bandgap metal oxide requires the introduction of defect energy levels that can either donate electrons (free carriers) to the attendant metal oxide conduction band (*n*-type conductor) or accept electrons from the metal oxide valence band (*p*-type hole conductor). In these oxides, the intrinsic conduction band is comprised principally of unfilled metal cation levels while the valence band is comprised of filled oxygen anion energy levels. Dopants are selected that can introduce energy levels that are either proximate to the conduction band minimum (CBM) or to the valence band maximum (VBM). Thus, for an *n*-type conductor, when aluminum is introduced as a dopant to zinc oxide under reducing conditions, the aluminum defect energy levels lie close to the conduction band minimum thereby allowing promotion of free carriers into the conduction band inducing a marked increase in conductivity. Based upon these electron band
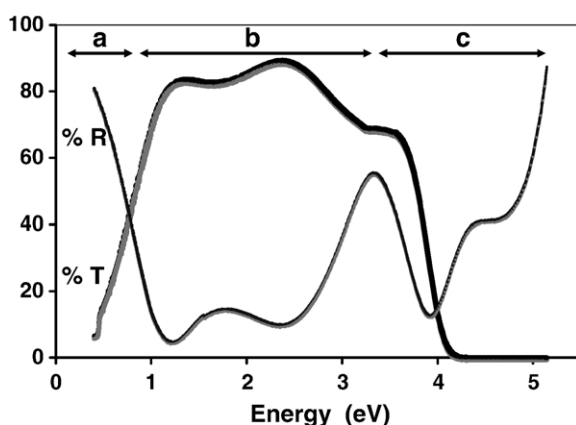

Fig. 1. Transmission (bold curve) and reflection (grey curve) spectra of a 160 nm thick *n*-type fluorine-doped tin oxide film sputter deposited onto a borosilicate glass substrate. The measured resistivity by a four-point van der Pauw measurement is 1.24×10^{-4} Ω cm. Region a is associated with free carrier absorption; region b is the high transmission passband in the visible spectral region; and, region c is associated with the strongly allowed absorption due to electron interband transitions (unpublished PNNL data).

structure considerations, a triad of empirical rules, summarized below, have been formalized and are useful for understanding TCO properties of these materials and selecting appropriate materials for TCO applications [20].

The first rule suggests that in order to achieve *n*-type conductivity in a wide bandgap metal oxide, the material should exhibit a relatively high electron affinity and concomitant low CBM. Thus, ZnO with an electron affinity of 4.35 eV and a direct bandgap energy of 3.37 eV would appear to be an excellent candidate for a conducting oxide that transmits visible light. However, MgO with an electron affinity of only 1.37 eV and a bandgap energy of 7.8 eV would not meet both criteria. While pure ZnO is an insulator, a slightly reduced form of the oxide contains oxygen vacancies; the extra electrons become associated with metal defect states near the bottom of the conduction band. As in the case of cadmium oxide discussed earlier, re-oxidation of the material will fill oxygen vacancies rendering the material insulating. This has been shown to occur in a cyclic voltammetry experiment where a thin film of ZnO functioned as the working electrode [21]. Upon cyclic polarization of the electrode in an electrochemical cell, ZnO was reversibly reduced and oxidized with associated resistivity change in response to the potential applied to the electrode. The chemical reactions associated with turning the conductivity on and off could be identified from the applied potentials. As is well known for this material, a more robust conducting state is readily achieved upon doping with trivalent metal cations such as aluminum, gallium, or indium. High defect concentrations also have been associated with a lowering of the CBM. However, conductivity at high carrier density will suffer due to a reduction in mobility that is caused by scattering of free carriers confined to the conduction band. If the conduction band exhibits a narrow energy distribution, increased scattering is likely and will decrease conductivity. Therefore, a wide distribution or dispersion of energy levels in the conduction band is to be preferred.

To achieve *p*-type conductivity, the second rule suggests that a material having a relatively low work function is required. This is a challenge for metal oxide systems since most are characterized by relatively large work functions due to the nature of the metal oxygen bond. Metal chalcogenides have somewhat lower work functions than the oxides making them better candidates for *p*-type wide bandgap semiconductors. However, certain transition metal oxides with incomplete d-shells will often show reduced work functions although weakly allowed optical transitions between the d-levels can somewhat degrade visible transparency. Candidate materials here include the delafossite oxides typified by $CuAlO_2$.

The third rule considers defect stability as a function of defect concentration. As more defects are added to a lattice in substitutional positions, the lattice can be prone to destabilization, possibly resulting in phase segregation. This is promoted by disparities in cation (anion) dopant sizes with respect to those comprising the base material. As the lattice distorts, the possibility for forming *killer defects* also will increase. Thus, in *p*-type doped materials, formation of anion vacancies can pin free carrier concentrations while in *n*-type materials, cation

vacancies become problematic. *Killer defect* formation, then, can be viewed as a response of the system to resist further insult to its structure and bonding arrangement. This consideration places restrictions on processing variables that can be chosen to mitigate *killer defect* formation. For example, to promote *n*-type conductivity, reducing conditions that create filled defect levels close to the CBM are desirable. Some materials can accommodate much larger defect concentrations before a structural response tends to drive the system back to a more stable equilibrium configuration with concomitant loss in conductivity.

Upon doping, the electron energy bands in TCO materials are subject to perturbation, in analogy to effects observed in doped silicon and other covalently bonded non-oxide systems. For example, when ZnO is doped *n*-type by introducing gallium into the structure, defect levels are introduced near the bottom of the conduction band thereby leading to an increase in the bandgap energy. The resulting blue shift in the high-energy absorption edge is known as the Burstein–Moss effect [22]. The magnitude of the shift correlates with carrier density and can be appreciable. Fig. 2 demonstrates this effect for a fully oxidized Ga:ZnO film that was subsequently reduced in hydrogen. The reduction process serves to extend the transmission window of the oxide to somewhat shorter wavelengths. However, since the free carrier absorption resonance (plasma frequency) scales with free carrier concentration, the optical transmission window begins to close at longer wavelengths. Conductivity and transmissivity are thus intimately related through these two effects.

2.4. Conduction pathways in free carrier TCO's

In a transparent wide bandgap metal oxide semiconductor, the conduction band is comprised principally of metal *n*s electron states where *n* is the principal quantum number of the unoccupied state. For large radii metal cations, significant

Fig. 2. A 250 nm thick 1 atm.% doped Ga:ZnO film sputter deposited onto a quartz substrate in an ambient 10 mTorr of O_2; the insulating film was fully oxidized. Upon post-deposition reduction with a 4% H_2/Ar mixture (1 atm) at 400 °C for 15 min, the *n*-type film resistivity dropped to 2.0×10^{-3} Ω cm. The Tauc's plot above shows a marked Burstein–Moss blue-shift of the band edge that results from introduction of free carriers into defect energy levels near the bottom of the conduction band (from Ref. [211]).

orbital overlap between adjacent cations can occur particularly when the counter anion (oxygen) is small in comparison with the metal cation. The extent of this overlap has been shown to be an important factor in driving conductivity in, for example, indium oxide where significant overlap of the 5s orbitals occurs [23]. More recent studies have shown that ternary metal oxide formulations containing zinc oxide (4s) also conform to this model where s-orbital overlap is a key factor in driving conductivity [24]. Based upon these considerations and those of the previous section, it would appear that oxides comprised of zinc, gallium, cadmium, indium, tin, and their binary or ternary mixtures should be ideal TCO candidates. Indeed, most highly conducting *n*-type TCO's have been derived from these materials and their related binary (ternary, quaternary) metal oxide mixtures.

From a practical standpoint, it is desirable to develop TCO materials that are amorphous because uniform films over large areas are desirable and amorphous layers are better suited to accommodate strain which is a necessary condition for enabling flexible electronics applications. However, traditional amorphous semiconductors (e.g. a-Si or a-As_2S_3) are neither highly conductive nor are they transparent. Based upon the orbital overlap criteria discussed in the previous paragraph, high conductivity in amorphous TCO materials can be expected since the orbital overlap of the s electronic states of spherical symmetry comprising the conduction band should be relatively invariant to disorder. Also, if strong overlap between these s states is maintained, the energy level dispersion associated with the conduction band can be large thereby promoting free carrier mobility. While materials like ZnO are very difficult to prepare in an amorphous state, several amorphous TCO materials already have been found that support the above contentions. These include amorphous-In_2O_3, and amorphous-Cd_2SnO_4 that are stoichiometrically related to crystalline bixbyite and spinel phases respectively. In the past several years, ternary amorphous oxide compositions that incorporate ZnO have been synthesized. In these materials, the Zn^{+2} 4s orbital contributes to the conduction path. Amorphous $InGaO_3(ZnO)_x$ compositions where $0 < x < 4$, show conductivities on the order of 100 S cm^{-1}, mobilities on the order of 10 cm^2 v^{-1} s^{-1} and carrier densities near 10^{20} cm^{-3} [25].

Electron energy band structure calculations based upon *ab initio* density functional theory have improved our understanding of free carrier transport in transparent conductors that is critical for the design of new systems [23,26]. Such calculations show the effects on band structure as dopants are incorporated into a base metal oxide. For example, the existence of a highly dispersed band near the bottom of the conduction band is common to all known *n*-type TCO materials. An example is provided in Fig. 3 for a conducting Sc:CdO material. The calculated band structure characteristics are useful for simulating optical absorption properties and determining the electron (free carrier) effective mass that influences carrier mobility [27–29]. Certain general trends become apparent from these calculations: the effective free carrier mass increases with atomic radius of the host oxide, and higher symmetry phases (e.g. octahedral cation coordination) tend to decrease effective carrier mass. It was also found that in comparing effective electron masses
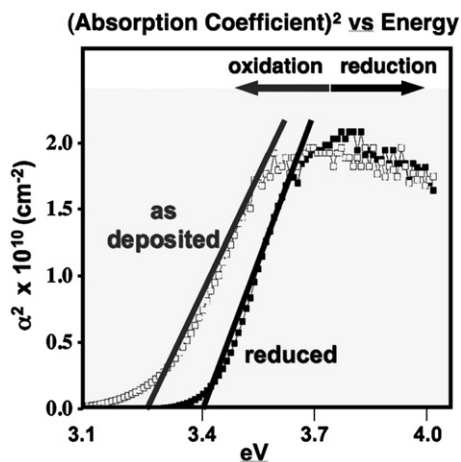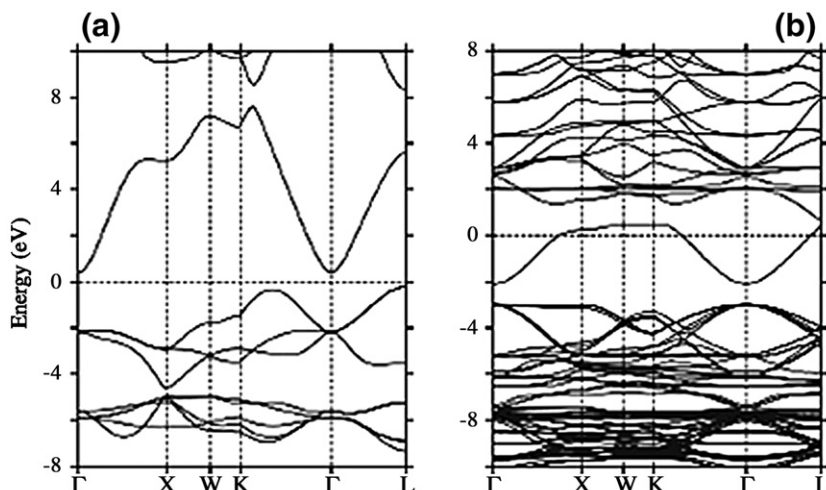
Fig. 3. The effect of doping on the calculated electronic band structure of scandium-doped CdO. (a) Undoped; (b) 12.5% Sc doped. Upon doping, the bandgap increases in energy (Burstein–Moss effect) and a high dispersion of levels near the CBM is seen. Data reproduced from reference [28]. The figures represent band energies as a function of position in the reciprocal unit cell (Brillouin Zone). The Γ point corresponds to zone center. For a detailed discussion of energy bands in crystals, the following reference may be consulted (Ü.Özgür, Ya.I. Alivov, C. Liu, A. Teke, M.A. Reshchikov, S. Dogan, V. Avrutin, S.-J. Cho, and H. Morkoç, J. Appl. Phys. (2005) 98, 041301).

in amorphous and crystalline ternary oxide phases that the effective mass did not appreciably change upon introducing disorder into the structure. Band structure calculations provide guidance for the development of metal oxide systems with increased transparency and conductivity.

2.5. Other conduction mechanisms

To this point, we have considered conducting mechanisms based upon generation and transport of free carriers in either the conduction band (electrons) or the valence band (holes) of a doped transparent oxide. Two additional conducting pathways can be envisioned in metal oxide systems. They are based upon the introduction, manipulation, and transport of localized charge states in an oxide host.

2.5.1. Electrides

A relatively new class of materials, termed *electrides*, has been reported earlier in large organic systems with cage-like structures [30,31]. These large molecules are referred to as cryptands since they inter metal cations in a tightly bound complex (crypt). In order to balance charge, the electron, initially associated with the alkali metal atom, is displaced to a different part of the structure where it becomes weakly trapped (~0.01 eV) within a supramolecular cavity. The materials can be cast as thin films. Movement between the cavities is thermally activated inducing conductivity. Alkali cryptands, notably K^+ (cryptand [2,2,2]) e^-, exhibit conductivities on the order of tens of Siemens/cm and while they absorb red and green light, do indeed transmit blue and near UV light [32].

An analog of these materials in metal oxide systems has recently been discovered [33,34]. Mayenite, a complex calcium aluminate of general formula $Ca_{12}Al_{14}O_{33}$ or 12 $CaO·7Al_2O_3$ or C12A7, is an insulator with high visible transparency. The chemical formula may also be written as, $[Ca_{24}Al_{48}O_{64}]^{+4}:2O^{2-}$,

where the former three-dimensional lattice framework consists of some 12 cages per unit cell. Fig. 4 illustrates the interconnected cage-like structure of this oxide. The oxide ions are referred to as *free oxygen* and occupy available cage sites. They also can be substituted with other anions (halide, hydroxyl) that then reside within the cages. The Hosono group has demonstrated that hydride anions (H^-) can be localized within the cages by high temperature hydrogenation of the base oxide. Upon irradiation of this material with ultraviolet light, a permanently conductive state resulted [35]. In analogy to the cryptands, the hydrogen anion loses its electron which becomes trapped within the cage structure
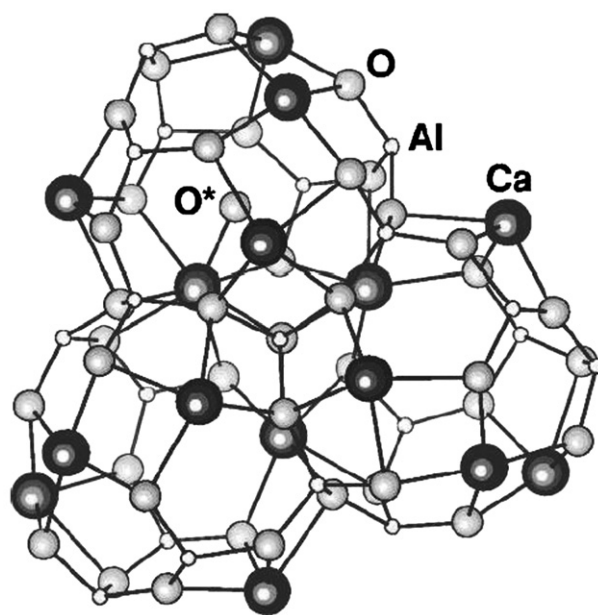

Fig. 4. Interconnected cage-like structure of mayenite, a calcium aluminate material identified as C12A7 showing the trapped oxygen anion at a localized cage site. Image abstracted from Ref. [224].

of the oxide. UV irradiation is necessary to promote this change separation which also is manifested by a marked increase in conductivity and appearance of a green–yellow coloration to the oxide. Such materials may serve as structures that promote conductivity by means of a hopping mechanism where charge carriers undergo activated site-to-site transport.

2.5.2. Polarons

Hopping of localized charge states among available sites in a lattice will also occur in mixed metal oxides where strong covalent interactions between metal cations and oxygen anions persist [36–41]. Fig. 5 is a schematic illustration of polaron hopping between adjacent sites in a mixed transition metal spinel oxide and shows the overall structure of the spinel unit cell that contains cations bound in both octahedral and tetrahedral sites. Since these states are localized, some amount of energy must be supplied to promote hopping and activate conductivity. Certain mixed transition metal spinel oxides (AB_2O_4) have been found to exhibit *p*-type conductivities on the order of 1000 S/cm [42]. The best materials to date contain nickel and either cobalt or rhodium [43,44]. In cubic $NiCo_2O_4$, cobalt is found to occupy both tetrahedral and octrahedral sites while nickel is found only in octahedral coordination [45,46]. Experimental measurements also indicate that both cobalt and nickel exist in di- and trivalent charge states on these lattice sites

suggesting that the simple formula above may better be represented as,

$$Co^{2+}_{1-d}Co^{3+}_{d}[Ni^{2+}_{d}Ni^{3+}_{1-d}Co^{3+}]O^{2-}_{4}, \qquad (0<d<1),$$

where both the nature of the ion and its charge state are allowed to vary on individual lattice sites. In this structure, nickel preferentially sits on the octahedral lattice sites (B) while cobalt can occupy both octahedral and tetrahedral sites (B and A).

Support for this contention derives from a considerable amount of data. X-ray diffraction measurements of $NiCo_2O_4$ powders and thin films show that the lattice constant increases with nickel content in the spinel oxide [45,46]. First principle DFT calculations using ultrasoft pseudopotentials were performed on cobalt spinel (Co_3O_4) and nickel cobalt spinel ($NiCo_2O_4$) [47]. When nickel was forced to sit in a tetrahedral lattice site, calculations indicated a small decrease in lattice constant. However, when nickel occupied octahedral sites, a marked increase in lattice constant was seen. The increase in lattice constant seen in the measured XRD data would seem to be indicative of nickel in octahedral coordination.

A strong covalent interaction between Ni^{+3} and O^{-2} to form $Ni^{+3-\delta}$ and $O^{-2+\delta}$ (where δ is the extent of charge transferred) defines the small polaron that acts to locally deform the lattice. Hopping activation energies are on the order of 0.02 eV and the
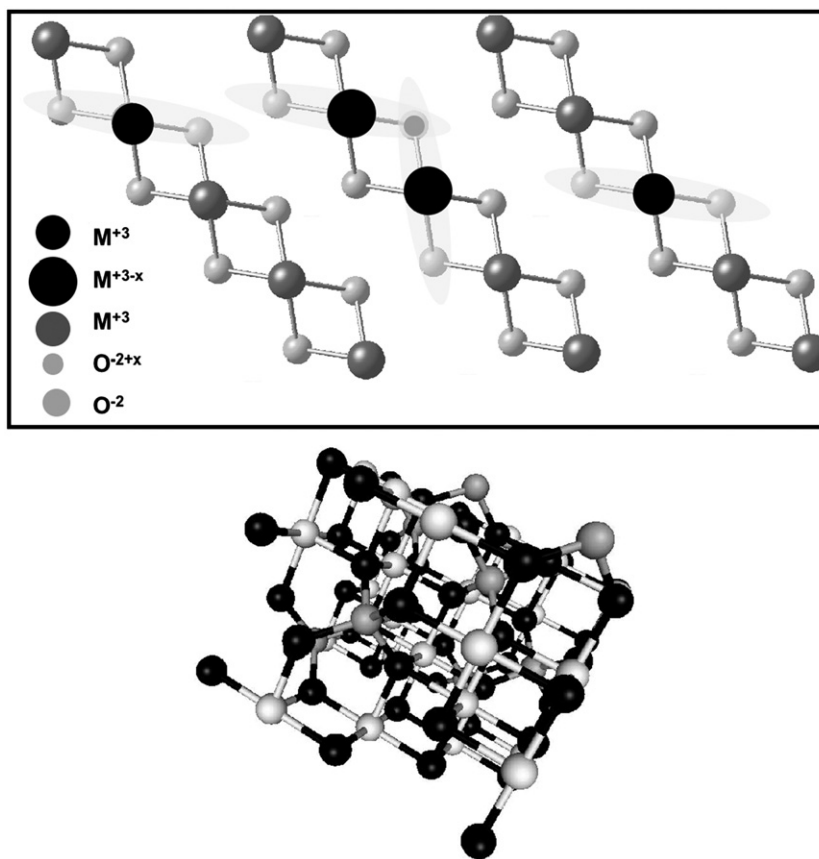

Fig. 5. Dynamic polaron hopping between nearest-neighbor sites in the edge-shared octahedrally coordinated cation-oxygen plane of the spinel oxide lattice AB_2O_4 (above). The hopping activation energy is dependent upon the magnitude of the polar interaction between the oxygen anion and metal cation, and the extent of cation site disorder resident in the lattice. The cubic spinel lattice accompanies the polaron hopping model and shows the octahedrally-coordinated cations (light grey), oxygen anions (black), and the tetrahedrally-coordinated cations (dark grey).

density of polarons scales with nickel content and with lithium content upon its introduction into the lattice [15]. While mobility is low, ~1 cm^2/V.sec or less, carrier density is quite high resulting in an appreciable conductivity. Weak optical absorption occurs in the visible region of the spectrum as seen in Fig. 6, but transmissivity is very high in the infrared to wavelengths as long as 16 μm. In addition to infrared transparency and reasonably high *p*-type conductivity, this material is also magnetic.

Guidelines for developing other polaron conducting oxides are based upon these results and are summarized below. As with other *p*-type conductors, oxidizing environments are found to promote conductivity while reducing environments are found to degrade conductivity. The low hopping activation energy in this material appears to correlate with cation site disorder arising from both the presence of mixed cations on lattice sites and the variability of oxidation states of those cations. For transition metal oxides of similar structure and stoichiometry, the bandgap energy generally increases as one progresses down a column of the periodic table. Thus, E_g for TiO$_2$ is about 3.7 eV, while for ZrO$_2$, and HfO$_2$, E_g is 5.5 eV and 5.8 eV respectively. Similar trends are seen for the two series (Sc$_2$O$_3$, Y$_2$O$_3$, La$_2$O$_3$) and (V$_2$O$_5$, Nb$_2$O$_5$, Ta$_2$O$_5$). This is in contrast to the behavior exhibited by the alkali and alkaline earth metal groups and the group IIIA metals beginning with aluminum. Band structure calculations for NiCo$_2$O$_4$ and the related spinel oxide where Rh substitutes for Co (NiRh$_2$O$_4$) also show a larger energy difference between the conduction band minimum and the valence band maximum [48]. Indeed, the rhodium substituted material exhibits not only a higher *p*-type conductivity than the cobalt nickel spinel but shows higher transparency in the visible region of the spectrum [49]. The unit cell volume also expands considerably when Ni or Rh replaces Co at octahedral lattice sites leading to lattice distortion and concomitant structural disorder that favors polaron hopping. Results suggest that

Fig. 6. UV/VIS/NiR transmission (bold curve) and reflection (grey curve) spectra of a 70 nm thick cubic spinel oxide of the composition NiCo$_2$O$_4$. Region a is associated with the near IR pass-band of the film, region b is associated with weak absorption due to d–d transitions of the transition metals, and region c is associated with strong absorption due to electron interband transitions. The optical response of this polaron conductor contrasts markedly with that of a free carrier conductor (Fig. 1) in that transmission increases markedly at longer wavelengths.

substitution of first row transition metal elements with elements deeper in the periodic table could lead to blue shifting of energy levels and higher visible transparency. The empirical trends discussed here, then, can help guide the design of polaron conducting TCO's with relatively high *p*-type conductivity.

3. Film deposition approaches

As described above, the theoretical emphasis on transparent conducting oxides has been focused on gaining an understanding of the parameters that simultaneously control electrical conductivity and optical transmission and to develop criteria that will decouple these parameters. In addition to understanding how these important parameters influence this phenomenon from a fundamental standpoint, the role of resident microstructure on properties cannot be overlooked, i.e. both the surface and the interface must be taken into consideration in order to improve the performance of transparent conducting oxides. This includes understanding how interfacial chemical interactions between the film and the substrate affect properties. Moreover, the electrical and optical properties are not only dependent upon the stoichiometry of the film but also upon the degree of residual stress present in the film and the attendant microstructure.

Many of the studies that are summarized here were published post 2000 following the appearance of a special issue of the Materials Research Society Bulletin that was focused on transparent conductors. Since then, several articles have also appeared that provided an overview of TCO film deposition technology [8,50–55]. For example, pioneering work by the group of Kawazoe and Hosono regarding the hole conductor, CuAlO$_2$, has positioned this class of materials at the forefront of transparent *p*-type oxides [56,57]; the work has recently been summarized in several publications [8,55,58]. One key aspect in TCO films of more recent interest which has been reviewed by Batzill and Diebold in 2005, addresses film surface properties, with respect to both surface electronic structure and surface chemistry [53]. Several articles also summarized activity on the very extensively studied doped ZnO materials [54,59,60].

The aim of this section is to summarize process-structure-property relationships in TCO films. The role of the interface, including grain boundary structure, and surface chemistry on TCO properties will be introduced and discussed in greater detail in a following section. Both solution and vacuum-based approaches to the deposition of TCO films are presented below. The vacuum techniques include evaporation, sputtering, and pulsed laser deposition, and the solution techniques include both sol–gel and an organic matrix approach.

3.1. Magnetron sputtering

Magnetron sputtering is a form of physical vapor deposition, which includes dc sputtering, radio frequency (rf) sputtering, and reactive sputtering [61–64]. A typical magnetron sputtering arrangement is shown in Fig. 7. This method appears to be the most popular technique for film deposition, owning to its cost effectiveness and capability for growing thin films on large area substrates; therefore, it became a somewhat conventional
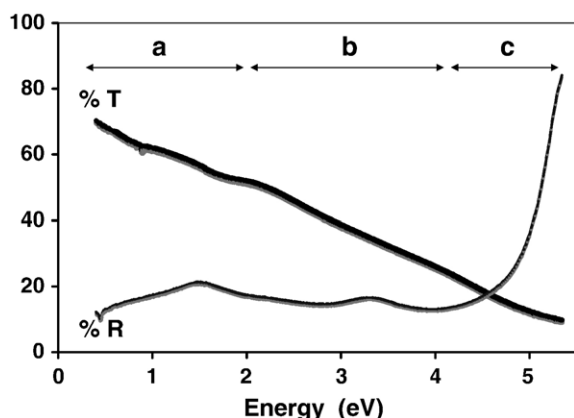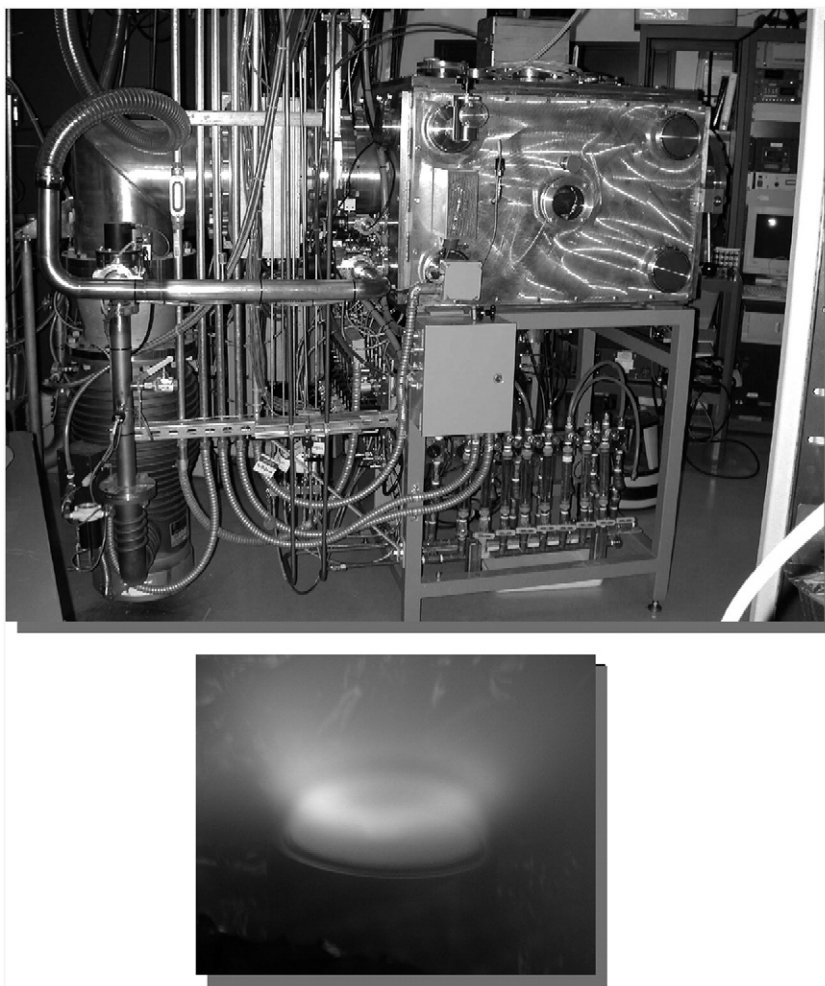
Fig. 7. A box coater sputter deposition chamber at Pacific Northwest National Laboratory (above). The rf plasma discharge from a 50 mm diameter spinel oxide target ($NiCo_2O_4$) viewed through the optical port also is shown. Substrates for coating are mounted on a rotary stage at a fixed distance above the target. For this deposition, 2 mTorr of a 50% O_2/Ar sputter gas mixture was used and the target substrate distance was 10 cm (Ref. [15]).

technique from a practical viewpoint to fabricate TCO films in this manner [5,65]. A large number of publications ($\sim 1/3$) with relevance to TCO do indeed pertain to this sputtering process. However, early applications of this method to deposition of TCO films were found to be quite costly, and sputtering was limited by low deposition rates, low ionization efficiencies in the plasma, and marked substrate heating effects which often led to inferior films [66]. Magnetron sputtering approaches were developed to help overcome these limitations. More recent developments have been made with a particular attempt to enhance deposition rates and to deposit films onto large area substrates through various technological improvements, such as closed field unbalanced magnetron sputtering, the use of variable field strength magnetrons, and pulsed magnetron sputtering [66–70]. Films prepared from magnetron sputtering in recent years include: n type — In_2O_3:Mo [71–73]; ITO [70,74–79]; In_2O_3:ZnO [80–83]; ZnO [84–97]; ZnO:Ga [98,99] and ZnO:Sc/Y [100]; p-type — $CuAlO_2$ [69,101–103], $NiCo_2O_4$ [15], (LaO)CuS [104–106], NiO [107], In_2O_3:Ag_2O [108], and several controversial ZnO-based materials [109,110]. A large area ITO film (30×40 cm^2) has been

deposited onto glass substrates by r.f. magnetron sputtering, which exhibited good uniformity and homogeneity [111].

An issue pertaining to TCO films deposited by means of magnetron sputtering concerned the observation that significant spatial variations in plasma composition were present during both reactive and dc sputtering. This may be the principal cause of the measured resistance heterogeneity that was determined in ZnO:Al films deposited from both oxide and metallic targets [93]. Recent developments [85] have overcome this limitation by employing simultaneous rf and dc magnetron sputtering to improve properties homogeneity over large areas in sputter deposited films; recent work has been detailed by Ellmer et al. in 1998 [112]. Considerable improvement of the resistivity distribution was observed ($\sim 5 \times 10^{-4}$ Ω cm) in 200 nm thick ZnO:Al films that were deposited onto glass substrates. To further mitigate such homogeneities that may lead to film composition and thickness inhomogeneity, plenary rotation of the substrate is often used.

Sputter deposition of TCO films can be combined with other film deposition methods to produce integrated multilayered stacks that comprise thin film solar cells. Thus, a multilayer CIGS (*c*opper *i*ndium *g*allium *di*selenide) cell structure has
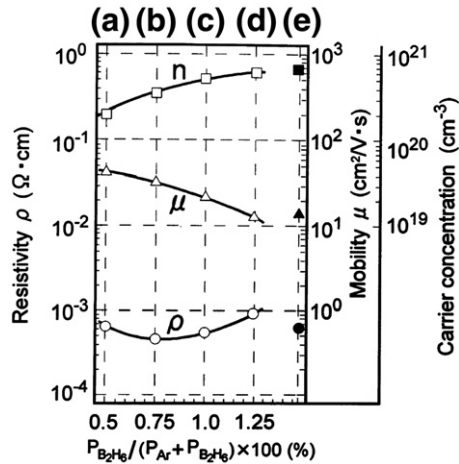
Fig. 8. A plot of the dependence of resistivity, mobility, and carrier concentration, on B_2H_6 partial pressure for ZnO:B films sputter deposited with no intentional heating of the substrate (black filled symbols represent data for a ZnO:Al thin film) [113].

been fabricated using both chemical bath deposition of a CdS layer onto which rf sputtered layers of ZnO were added [113]. Sputtering yielded a thin insulating ZnO buffer layer onto which doped and conducting Al:ZnO and B:ZnO layers were added. Sputter targets included both ZnO and alumina doped ZnO while boron doping was achieved by using a B_2H_6/Ar sputter gas composition. Analysis of the dependence of sputter gas composition on electrical properties was used to optimize the deposition parameters. An antireflection MgF_2 layer completed the stack. Shown in Fig. 8 is the dependence of resistivity, mobility, and carrier concentration, upon the B_2H_6 reactant gas partial pressure for ZnO:B films deposited unto unheated, transparent substrates (the solid symbols represent data associated with a ZnO:Al thin film).

3.2. Pulsed laser deposition

Pulsed laser deposition, shown in Fig. 9 is a very effective thermal technique for the preparation of epitaxial films in moderate vacuum, or under ultrahigh vacuum conditions if desired, and is applicable to the deposition of a wide variety of oxide materials, including TCO materials [114,115]. It is the deposition method of choice when multicomponent compositions that are phase pure are required. In a typical PLD process, a focused train of high energy laser pulses, derived from a UV nanosecond pulsewidth laser source, such as the frequency tripled (355 nm) or quadrupled (256 nm) solid state Nd:YAG laser, or the KrF (248 nm) or ArF (193 nm) excimer laser, is rastered over either a metal, a single crystal oxide, or a compressed oxide powder target in a vacuum chamber. A suitable substrate, often heated, is brought into contact with the laser plume (formed by the high pulse energy beam–target interaction) that is comprised of atomic and molecular species ablated from the target. Typically, for TCO film deposition, the substrate temperature is maintained between 450 and 700 °C, and the oxygen partial pressure is usually kept below several millitorr. The oxygen partial pressure in the chamber is key to actuating the n-type conducting property of these metal oxides in that low partial pressures promote formation of oxygen vacancies which generates free carriers. For metal targets, the oxygen content of the chamber can be carefully regulated to promote formation of a targeted flux of oxygen radicals in the laser plume resulting in the appropriate oxygen deficient metal oxide film. This concept was exploited in the fabrication of ZnO: Al [116]. Although very high deposition rates up to ∼600 μm/ h have been reported, rates on the order of ∼1 μm/h are more typical when high quality, epitaxial thin films are desired. For example, at a laser pulse repetition frequency of 10 Hz, a wavelength of 193 nm, a pulse energy of 2 to 3 J/cm^2, and oxygen partial pressure of several millitorr, deposition of doped ZnO films from ceramic targets will occur at a rate on the order of about 10 nm/min at a target substrate distance of 30 mm. Post deposition annealing in oxygen is often required for p-type TCO's because the deposition often occurs under reducing conditions at elevated temperatures. Recent publications on films prepared by PLD include: ITO [117–120], TiO_2 [121,122], ZnO [116,123–132], and p-type TCO [8,58,133–136].
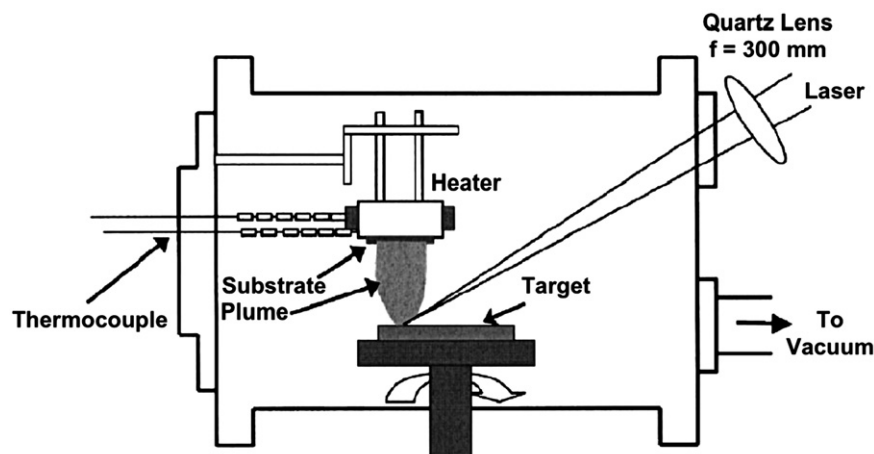

Fig. 9. Schematic view of a pulsed laser deposition system [132]. Provision is made for controlling the ambient atmosphere within the chamber and substrate heating. Short wavelength irradiation of the target material creates an ablation plume that contacts the substrate.

Bhosle and Narayan investigated the role of substrate behavior and deposition conditions on the electrical and optical properties of Ga:ZnO films [126]. The nature of grain orientation and grain boundary morphology that resulted from various deposition conditions, was found to play a significant role in carrier concentration and the mobility in thin films deposited on glass substrates. They explained this correlation in terms of trapping of electrons and buildup of a potential barrier across the grain boundaries. A rather low electrical resistivity ($\sim 1.9 \times 10^{-4}$ Ω cm) was obtained with Ga:ZnO films on glass substrates through optimization of the substrate temperature and attendant oxygen pressure, which was comparable to that of epitaxially deposited films on sapphire substrates ($\sim 1.4 \times 10^{-4}$ Ω cm) [126].

The PLD process is versatile and is amenable to coupling with ultraviolet irradiation [137], oxygen radical assisted deposition [116], or magnetic field promoted deposition [124]. Thus, a magnetic field perpendicular to the laser plume was useful in preparing Al:ZnO through coupling with the PLD process. Deposited films exhibited a markedly low resistivity of 8.54×10^{-5} Ω cm and an average transmittance exceeding 91% over the visible wavelength range. The authors argued that the low resistivity was due to the fact that crystal growth disorder that originated at the film substrate interface could be suppressed through application of an external magnetic field that interacted with the plasma plume thereby yielding an increased mobility. C-axis orientation was promoted at the substrate, giving rise to the observed increase in mobility [123,124].

Thus far, PLD has been the primary technique used to deposit TCO films that exhibit exceptionally low resistivity on the order of 10^{-5} Ω cm [123,124,138,139]; however,

magnetron sputtering results in films having resistivity several times greater than those derived from the PLD process. Sahu and Huang [140] predicted the electrical resistivity on the order of 10^{-5} Ω cm in multilayered ZnO/Ag/ZnO films; unfortunately the measured value was not provided.

3.3. Chemical vapor deposition

The most common thin film deposition method in advanced semiconductor processing involves thermally induced decomposition of a film precursor molecule as the volatile species interacts with a hot surface. The decomposition product then deposits on the substrate surface. In a typical CVD process, gaseous reactants from selected precursors often are directed through an activated environment (high temperature, light, or plasma), which acts to dissociate the precursor molecules. Films deposit onto heated substrate surfaces to yield the desired films and targeted morphology. The deposition of thin films often involves heterogeneous chemical reactions that occur on/near the vicinity of the substrate surface [141]. This technique has been used to form semiconductor films (crystalline and amorphous), insulators, and metals. Variations of this processing method include Atmospheric Pressure CVD (APCVD), Low Pressure CVD (LPCVD) and Plasma Enhanced CVD (PECVD).

Metalorganic chemical vapor deposition (MOCVD) uses organometallic precursors (Fig. 10) that decompose when heated to form metal oxides, which then deposit as films. Under appropriate growth conditions, epitaxial layers can be realized [23,142–144]. Variations of this method include oxygen plasma assisted (OPA) MOCVD where, under high vacuum, extremely
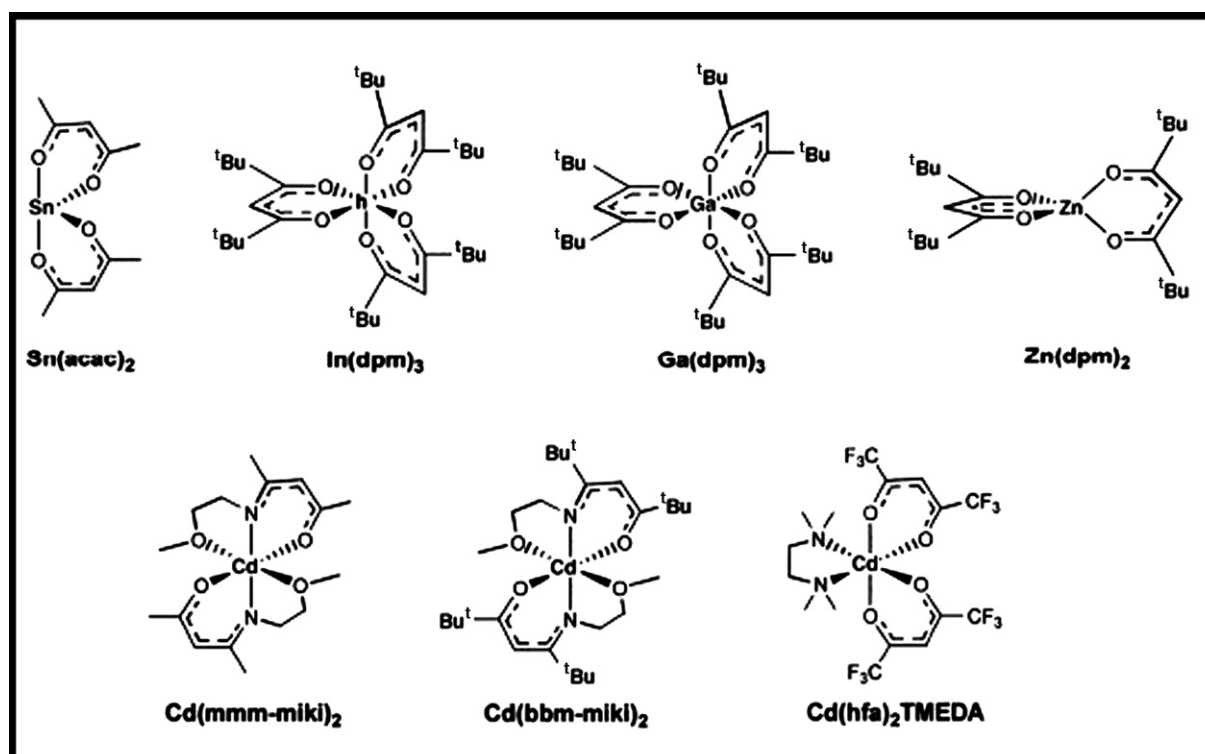

Fig. 10. A collection of volatile organometallic precursors used in MOCVD processing of TCO films.

low defect density and high chemical purity oxide films can be grown. In many cases, MOCVD does not necessarily require high vacuum and deposition can indeed occur at moderate pressures (2 to 100 kPa). As a result, MOCVD has become a preferred process for the fabrication of compound semiconductor films. The primary limitation of the MOCVD process is associated with purity and cost of preparation of the requisite metalorganic precursors, which in many cases tend to be extremely reactive, and hence require careful handling and often purification by thorough recrystallization or sublimation procedures. In addition, most metalorganics are volatile and quite often very toxic, thus requiring extraordinary handling procedures. However, films derived from this method can be of high quality both chemically and structurally. Several examples follow to demonstrate this approach.

In order to improve the performance of solar cells based upon p-type CuInSe$_2$, ZnO films have been used as a replacement buffer layer for CdS which is located adjacent to the active selenide layer [145]. Here dimethyl-di(diethylamino) zinc was used as the zinc precursor while tetrahydrofuran served to introduce oxygen into the system. Following a programmed deposition schedule (Fig. 11) that involved controlling the ratio of the zinc and tetrahydrofuran precursors and the substrate temperature, a high purity wurtzite phase of ZnO was formed on the chalcogenide substrate; the film exhibited a random crystallite orientation and showed compressive stress. X-ray photoelectron spectroscopy (XPS) sputter depth profiling indicated that some diffusion of indium into the film from the underlying active layer had occurred, likely forming an interstitial layer of higher conductivity that the remainder of the film. From this work, the importance of film substrate interaction
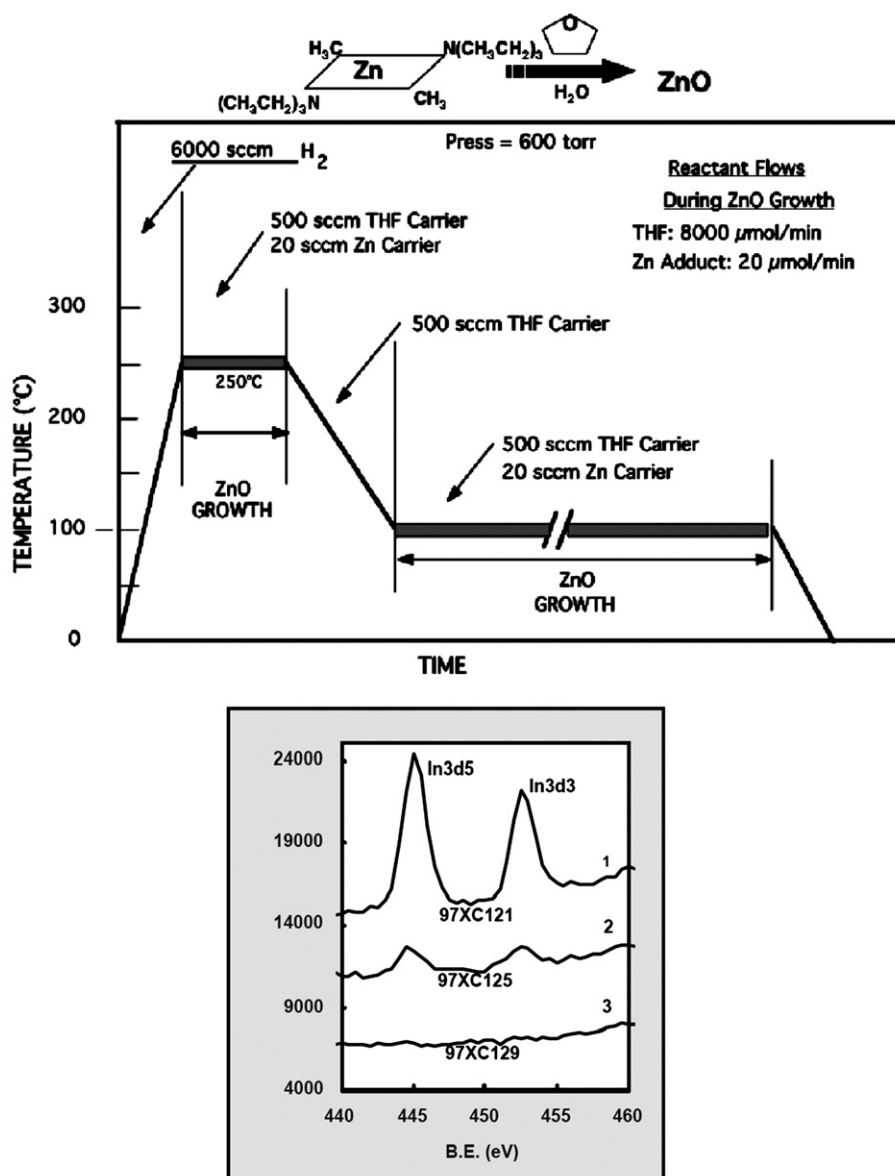

Fig. 11. Run schedule for CVD growth of ZnO films on CuInSe$_2$ substrates that includes two growth regimes (above). Sputter depth XPS profiles (right) of a deposited zinc oxide bilayer showing indium diffusion from the substrate into the film during stage 1 growth. Spectra 1, 2, and 3, correspond to a film thickness of 10, 20, and 80 nm respectively (Ref. [145]).

cannot be overemphasized and should be investigated with respect to film properties alteration.

While not a great deal of attention has been devoted to the preparation of cubic CdO films by this method owing to toxicity concerns of the precursors, published work demonstrates the efficacy of this method for controlling film properties and morphology [146,147]. By means of MOCVD using dimethyl cadmium as a precursor, the properties of deposited films were found to be very sensitive to deposition temperature from about 100 °C to 450 °C. Below about 250 °C, randomly oriented crystallites formed on heated glass substrates. At higher deposition temperatures, crystallites with a preferred (200) crystal orientation resulted, and at higher temperatures, a highly oriented crystalline morphology with nearly perfect intragrain structure was formed. The *n*-type nature of the conductivity was found in all cases, but increasing deposition temperature was also found to markedly improve free carrier mobility while decreasing carrier concentration.

In another example, CVD approaches were used to deposit binary metal oxide films based upon CdO and SnO_2 [148,149]. Two stable crystalline phases in this system are the orthorhombic and rhombohedral $CdSnO_3$ (perovskite) structures and the more promising cubic spinel $SnCd_2O_4$ structure owing to the observed increased carrier mobility and relatively low absorption at visible wavelengths. In reported work, mixtures of both perovskite and spinel structures have been found with films often containing multiple compositions represented by $Sn_xCd_{2-}O_{2x+y}$, where $0<x<1$, and $0<y<2$. In these multiple phase containing films, marked variations in both carrier density and carrier mobility have been noted. The optical band gap also blueshifts upon incorporation of more tin oxide in the film. With appropriate choice of precursor and deposition parameters, amorphous phases can also be formed. CVD approaches can be technologically important in the fabrication of both crystalline and amorphous large-area coatings.

3.4. Solution deposition

Two contrasting chemical routes can be used for the deposition of oxide films. The traditional sol–gel process drives the evolution of inorganic networks through the formation of a colloidal suspension (sol), and gelation of the sol to form a network in a continuous liquid phase (gel) as described in Fig. 12. Following spin casting or dip coating, post-deposition thermal treatment consolidates the network forming a continuous oxide phase. Multiple layers can easily be added leading to densification and improvement in properties [150]. The precursors for synthesizing these colloids consist of a metal or metalloid element surrounded by various reactive ligands. Metal alkoxides are most popular because they react readily with water to form the metal oxide. The most widely used metal alkoxides are the alkoxysilanes, such as tetra-methoxysilane (TMOS) and tetraethoxysilane (TEOS). However, other alkoxides based upon aluminum, indium, tin, titanium, zinc, and boron compositions are also commonly used in the sol–gel process. For deposition of TCO films, metal acetates also have been used. Precursors usually are dissolved in alcoholic solutions having a targeted initial pH. Slow hydrolysis produces an extended oxide network that is transferred to a cleaned substrate by dipping or spin casting procedures. Post deposition heating removes the organic constituent and forms the metal oxide. A series of zinc oxide/alumina films was prepared by this method to confirm the supposition that alumina additions to ZnO leads to a blue shift in the measured bandgap energy [151], as shown in Fig. 13.

An alternate solution-deposition approach is based upon a reduction-oxidation (REDOX) reaction. In this case, metal nitrates, serving as oxide precursors, are dissolved in water (or alcohol) with a suitable organic complexing agent such as glycine (water soluble), NH_2CH_2COOH, or malonic acid (alcohol soluble), $HOOCCH_2COOH$. The organic molecule forms a complex with the metal cations present and, as the solvent evaporates during spin casting or dip coating, forms an amorphous organic film that entrains the nitrate anions. Moderate heating causes nitrate oxidation of the organic material thereby rendering the stoichiometric oxide film [152]. The process also is quite useful for the preparation of narrow size distribution ceramic powders that can be compressed into targets for PVD and PLD deposition of thin films [153]. This method is particularly useful for depositing

Acid-Catalyzed
Linear chains formed with length controlled by pH.
(higher density films result)

Base-Catalyzed
Branched chains formed to create more open network.
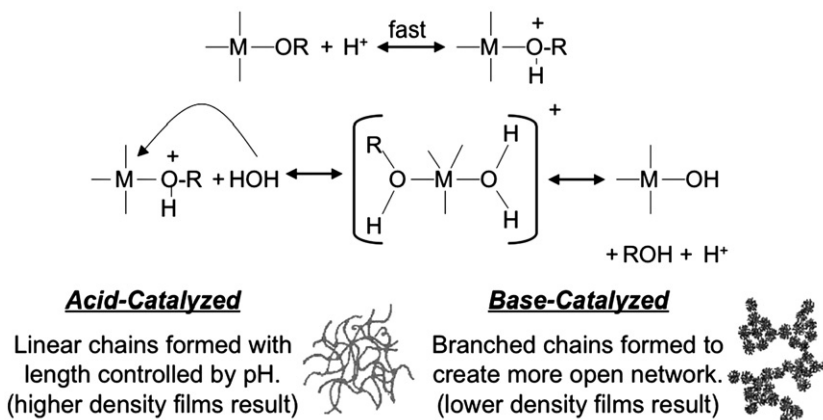(lower density films result)

Fig. 12. Sol–gel chemistry involves acid (or base) catalyzed hydrolysis of a soluble chemical precursor that then condenses with itself to form an extended network. Solution pH influences the subsequent film density following post deposition annealing to remove the residual organic constituents.
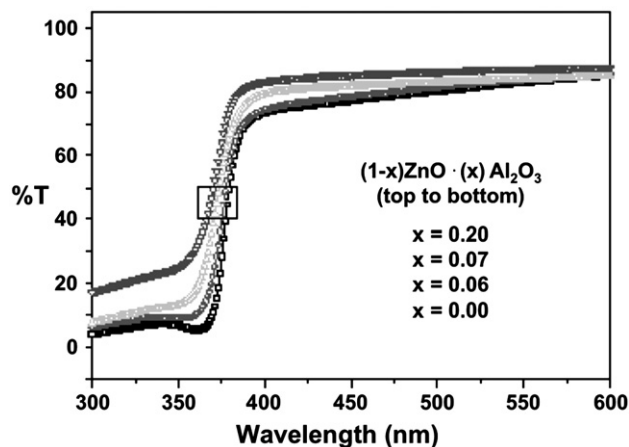
Fig. 13. A series of zinc oxide/alumina films was prepared by the sol–gel process, showing that alumina additions to ZnO lead to blue-shifts in the associated bandgap energies [151].

stoichiometric films of homogeneously doped oxides, and of binary, and ternary metal oxide films. For example, compositional spreads of the p-type polaron conductor $NiCo_2O_4$ are easily derived by adjusting the metal nitrate composition in the precursor solution. Upon heating in air, the spinel phase evolves and conductivity on the order of 1000 S/cm can be realized for the aforementioned material [154].

Solution deposition is attractive mainly because of its simplicity and low cost. In addition, the rich chemistry of sol–gel processing coupled with pyrolysis enables the fabrication of a variety of complex oxide compositions [155,156]. Compared to vacuum based approaches described in the other sections, solution processing has not been considered as a technique that will produce high quality thin films, with respect to control over the texture, growth rate, composition, and microstructure of deposited films. However, the low cost of preparing films using this approach is attractive from a commercial standpoint.

Solution deposition offers an additional unique advantage as it enables deposition of composite, or so called "hybrid", films. For example, Ag particles have been embedded into ITO films to reduce the resistivity, while maintaining transmittance, by spin coating a Ag-containing ITO sol [157]. A low resistivity $\sim 2 \times 10^{-4}$ Ω cm was observed with a silver ion concentration of 0.05 M in the sol; the transmittance of this hybrid film is greater than 80% in the visible region of the spectrum. Transparent inorganic–organic n-type thin film transistors have recently been fabricated by combining In_2O_3 thin films with nanoscale organic dielectrics [158], which resulted in a large field-effect mobility ~ 120 cm^2/Vs. The hybrid integration may enable a new approach to fabricate wide band gap metal oxide semiconductors with other transparent organic compounds to achieve unique optoelectronic devices.

The REDOX glycine-nitrate method also is extremely useful for deposition of hybrid metal/metal oxide films. In reported work, uniform gold spheres on the order of 10 nm in diameter have been co-deposited with ZnO from solution. Such films can act as sensors since the work function of the hybrid film is

dependent upon the nature of the adsorbed analyte and the film resistivity scales with the amount of analyte adsorbed on the film. This has been demonstrated for such hybrid films when used as the active sensing layer in a field-effect transistor [159]. Fig. 14 shows the response of the CHEMFET (CHEMical Field Effect Transistor) device upon exposure to air containing cumulative amounts of ammonia.

3.5. Spray pyrolysis

Aerosol spray pyrolysis (SP) is the process by which a precursor solution is atomized to form droplets, which are then carried by a flowing gas through a heated reactor (Fig. 15). Inside the reactor, the solvent evaporates and the solutes become thermally pyrolyzed at the surface of a heated substrate yielding a film having the requisite oxide phase and well-characterized film morphology [160,161]. SP combines the advantages of both solution-to-solid and gas-to-solid processing. This is particularly critical for fabricating high purity multicomponent compositions, because one atomized droplet from the initially homogenous solution most often results in one submicrometer sized particle, insuring stoichiometric invariance from the solution composition. Therefore, SP has been explored not only for the synthesis of complex oxides including superconductors and piezoelectrics, but also multicomponent TCO film compositions.

With respect to producing homogeneous films, SP is well suited because it can lead to the deposition of films having the desired stoichiometry on large substrates with intricate or high aspect ratio geometries (e.g. wires). Deposition conditions can be varied to produce films with controllable porosity and hence, variable refractive index. Pioneering work was carried out by Chamberl and Skarman in 1966 in which they deposited conducting and transparent CdS films for solar cells by a spray pyrolysis method. Further work was carried out by Prince, et al., regarding the preparation of In_2O_3 [162]. They investigated In_2O_3 properties as a function of spray pyrolysis parameters,
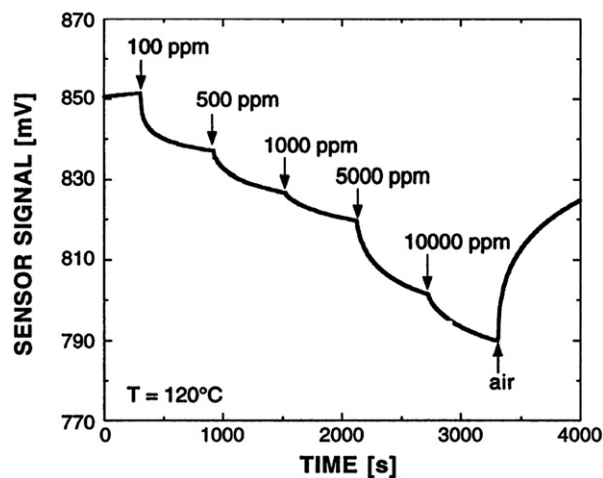

Fig. 14. The measured work function response of a 250 nm thick ZnO film containing 20 nm diameter gold particles at a loading of 2 vol.% (CHEMFET) upon exposure to ammonia vapor at 120 °C (Ref. [159]).
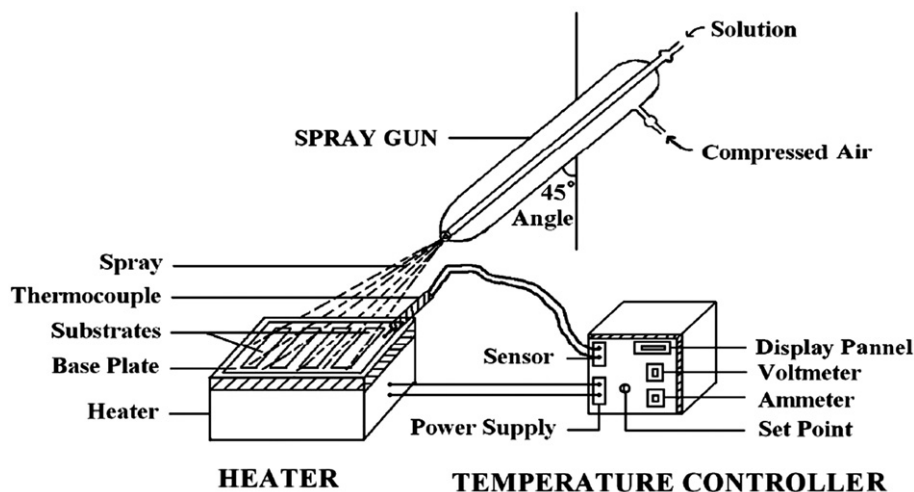
Fig. 15. A diagram of the apparatus used for the spray pyrolysis deposition of thin films [182].

including the concentration of precursor chemicals in the spray solution, the ethanol/water ratio that affects the reducing nature of the ambient atmosphere, the air-flow rate, the substrate-nozzle distance and the substrate temperature. Electrical and optical properties of other TCO films have been investigated recently on spray-pyrolyzed In_2O_3 [162–167], SnO_2 [168–172], CdO[173–175], and ZnO [176–180].

Among these variables, the substrate temperature (T_s) has long been considered as the most important factor in producing high quality thin films from SP processing, because it influences droplet drying, decomposition, crystallization, and grain growth during the film deposition process. T_s was found to affect both the crystallinity and the preferred orientation in In_2O_3 [162–164] and ZnO [178]. Amorphous films are expected at very low T_s, whereas a high T_s promotes crystallite grain growth and loss of preferred orientation. Prince et.al. [162] observed a resistivity minimum, which was attributed to a maximum of both carrier concentration and mobility at $T_s=380$ °C. They proposed that the mobility maximum was due to a reduction in grain boundary scattering. A large discrepancy exists in reported grain size, preferential orientation, and electrical properties of spray pyrolyzed In_2O_3 films [162–164], which likely is due to differences in the stoichiometry of In_2O_3. The spray pyrolyzed ZnO films were found to have a preferred (002) orientation [177,178]; however, doping with Al perturbed both the texture and crystallite orientation of the films that likely resulted from the presence of interfacial stress formed by the difference in ionic size between Zn^{2+} (0.074 nm) and Al^{3+} (0.054 nm) [177,180].

As mentioned above, SP is a simple, scaleable, and cost effective process for fabricating complex oxides, such as fluorine doped SnO_2 films. Manifacier et al. reported fluorite doped SnO_2 in 1979 [181]. Several publications have been reported recently, in which different precursors of Sn and F were explored. Similar electrical and optical properties were observed in spray pyrolyzed SnO_2:F thin films with a variety of precursors [170,182–184].

A breakthrough was documented by Veluchamy et al. in 2001, who reported highly transparent and conductive F doped SnO_2 on glass substrates as large as 82×71 cm^2 with $(CH_3)_2$-$SnCl_2$ and NH_4F/HF used as the precursors. Typical films exhibited a mobility of ~ 44 cm^2/Vs, carrier density (donor) of 3.5×10^{20}/cm^3, electrical conductivity ~ 2500 S/cm, and average transmission $\sim 85\%$ in the wavelength range from 400–1000 nm. A solar energy conversion efficiency was observed to be $\sim 15\%$ for a 1 cm^2 cell with CdS/CdTe on a spray pyrolyzed SnO_2:F substrate.

3.6. Combinatorial deposition methods

The ability to deposit compositional spreads of multicomponent oxide formulations in a single deposition run is attractive for investigating the complex phase space associated with ternary oxide compositions typified by $(In_2O_3)_x.(Ga_2O_3)_y.(ZnO)_z$. Both sputter deposition and PLD approaches have been successfully used to deposit spacewise varying compositions of many materials including oxides in one or two dimensions from two or three target systems [25,29,185–188]. Two examples are presented to illustrate the efficacy of this approach.

Sputter deposition of the infrared transparent p-type conducting oxide based upon cobalt nickel spinel ($NiCo_2O_4$) has been successfully demonstrated in a two-target system where both DC magnetron sputtering from metallic targets in oxygen or RF magnetron sputtering from metal oxide targets in an Ar/O_2 ambient have been used [15]. The respective 50 mm diameter targets Ni (or NiO) and Co or (Co_3O_4) were mounted in a box coater chamber and each was canted at an angle ($\sim 30°$) with respect to the substrate normal. Silicon, glass, and sapphire substrates (25 mm wide and 225 mm long) were mounted adjacent to each other a distance of 250 mm above the targets. Following evacuation, a several millitorr Ar/O_2 gas mixture was admitted to the chamber and a plasma discharge was initiated. Films were deposited and characterized as a function of target-substrate distance, partial pressure of oxygen in the mixture, nature of the substrate, and plasma conditions. Following deposition, film composition was determined from measured XPS spectra as a function of position relative to the two targets; film conductivity was also measured as a function of position (Fig. 16). Correlation between these two data sets allowed an
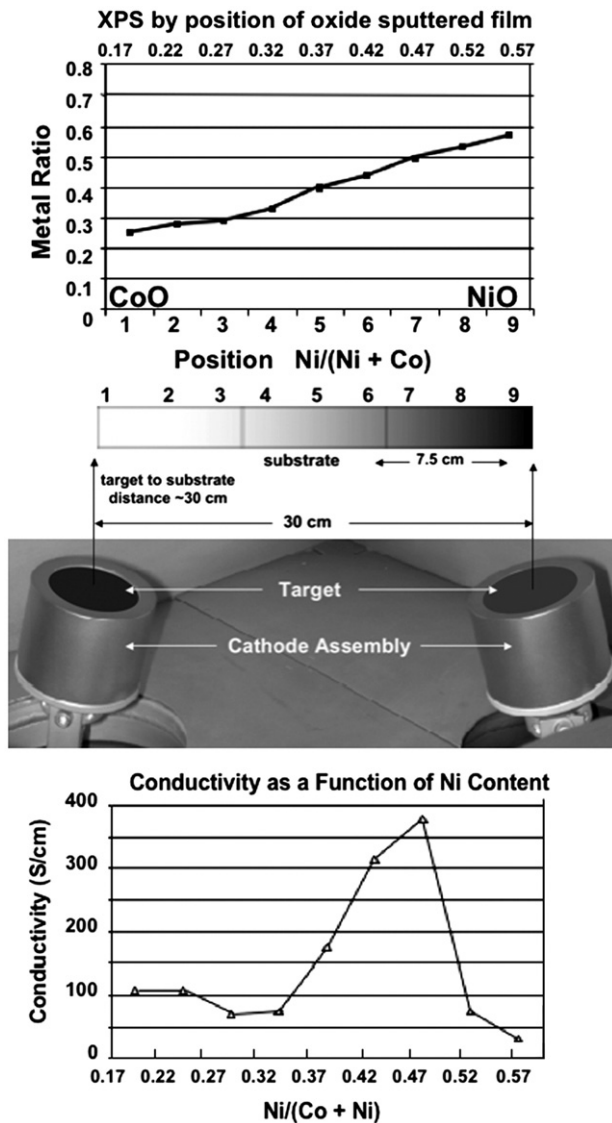
Fig. 16. Combinatorial sputter deposition target deployment for preparing NiCo$_2$O$_4$ films using Co$_3$O$_4$ (left) and NiO (right) targets; composition spread (top) and correlation of composition with resistivity (bottom) also are shown (Ref. [15]).

optimum composition corresponding to highest *p*-type conductivity to be readily determined. X-ray diffraction and Raman spectroscopy were also carried out to verify phase purity. The spinel phase formed over the continuous composition range from 0 atomic % nickel to 50 atomic % nickel. At higher nickel contents, phase separation into a spinel and cubic nickel oxide phase occurred with concomitant loss in conductivity. This approach is conducive to rapid determination of structure property relationships in multicomponent oxide systems and effectively allows quantification of phase stability regions of the system.

A PLD approach was selected for investigating composition-conductivity correlations in the ternary TCO oxide, (In$_2$O$_3$)$_x$ (SnO$_2$)$_y$(ZnO)$_z$. In this previous work, a pseudo ternary phase diagram was investigated in which two of the end members were indium tin oxide with different indium tin ratios [189].

Three moveable targets in a triangular geometry could be selectively irradiated with a fixed number of laser pulses. Following irradiation of one target that was positioned to deposit material off the center of the substrate, a new target could be rotated into position with concomitant rotation of the substrate to expose a different region to the ablation plume. Repeated cycling of targets and substrate allowed a compositional spread to be developed in two dimensions thereby effectively producing a two-dimensional phase diagram in the deposited film. Analysis of the film with respect to composition and conductivity, then, established the desired correlation as seen in Fig. 17. Film transparency also could be determined for spatially isolated regions of the deposited film by means of small spot UV/VIS spectroscopy. A correlation between composition, conductivity, and transmittance could then be developed for this ternary oxide deposited in a single deposition experiment.

Combinatorial deposition has developed into a generally accepted technique that promotes rapid characterization of film properties as a function of composition. The technique is amenable to both PLD and PVD film deposition approaches.

4. Carrier mobility in TCO films — Theory and practice

Over the past three-dozen years, a marked improvement in conductivity for transparent doped metal oxide systems has been registered as seen in Fig. 18. However, the measured resistivity of these oxide films appears to approach a limiting minimum value of about 10^{-4} Ω cm. Several approaches to further minimizing resistivity have been discussed above and include tailoring compositions, promoting composition homogeneity, developing amorphous phase materials, engineering the defect chemistry, minimizing film–substrate interactions, and controlling microstructure. For example, a ZnO film will chemically react with a borosilicate glass substrate to form a zinc borate compound as seen by the Raman spectrum of the post-deposition annealed film as seen in Fig. 19. All of these actions either directly or indirectly indeed influence carrier mobility and in turn, the conductivity. Further improvement in
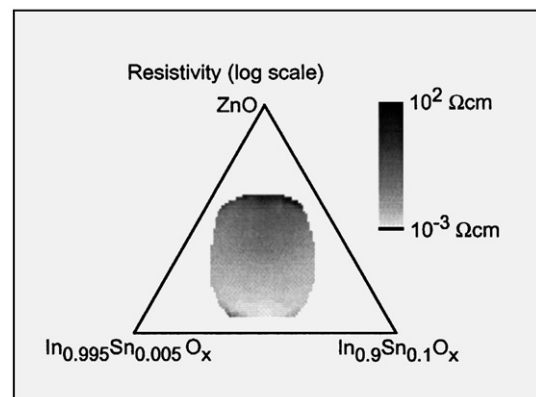

Fig. 17. Combinatorially derived resistivity phase diagram of a PLD deposited pseudo-ternary composition showing marked changes in film resistivity as a function of composition (Ref. [189]).
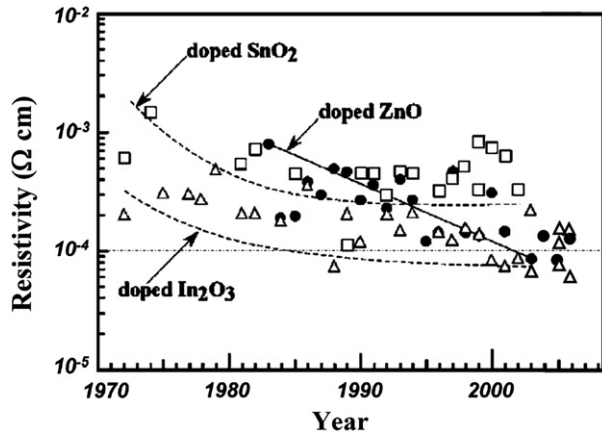
Fig. 18. Reported resistivity of doped In_2O_3, SnO_2, and ZnO TCO films with time (a revised plot after Fig. 2 by Minami [5]).

TCO properties, then, must necessarily concentrate on approaches to increase carrier mobility.

4.1. Hall mobility in an n-type TCO

Compared to semiconductivity or superconductivity, the phenomenon of electronic conduction coupled with optical transparency demands a more comprehensive understanding. A rigorous underlying physical explanation for the coexistence of conductivity and transparency is still sought [190]. Hence, much research on improving the properties of TCO films has been primarily undertaken on an empirical basis. Since the theory is not fully developed for single crystal materials such as ZnO or In_2O_3, the influence of attendant polycrystalline microstructure on the properties of these films remains elusive. In the published literature, conductivity and optical transmittance for the same film material can vary significantly. While film transparency in the visible spectral region is usually reported in the range of 80%–90%, discrepancies, abound in the measured Hall mobility values that can vary over the range from 5 to 150 cm^2/Vs, even in films having similar carrier concentrations.

Band structure calculations have revealed that the mobility in n-type TCO films is strongly dependent upon the characteristics of the conduction band. The width of the conduction band, comprised principally of metal ns states, will influence free carrier scattering, and hence, mobility. The magnitude of the band overlap between metal ns orbitals on adjacent cations may also partially explain the high mobility in terms of the presence of continuous electron conduction paths between these states [3,191,192]. Even though the band structure diagram provides insight into the physical origin of high mobility in doped semiconductors, it cannot provide quantitative information regarding carrier mobility, particularly for heavily doped oxide films. The ionized dopants that contribute free carriers to the conduction band, have long been associated with scattering centers, as formalized by Conwell and Weisskopf [193], who treated the scattering as uncorrelated collisions in a truncated Coulomb potential of ionized dopants. Further improvement was made to this model that incorporated the concept of a

screened Coulomb potential, which considered the screening of the ionized impurities by mobile charge carriers (Brooks–Herring–Dingle theory) [194]. It is now known that the limitation of the mobility by ionized impurity scattering is valid only for well-grown homogeneously doped films with carrier densities greater than 5×10^{20}/cm^3.

Ionized impurity scattering alone cannot explain measured Hall mobilities in TCO films. Other scattering mechanisms must be taken into consideration, such as polar optical-phonon scattering, acoustic-phonon scattering associated with deformation potentials, and piezoelectric interactions as described by Makino [195], Ellmer [54], and Look [196]. The calculated mobilities may still not yet be comparable to measured values due to variations in both the crystalline and microstructural nature of TCO films [5,54]. Lowney and Bennett [197] derived, from first principles, a mathematical description of electron mobility in GaAs with consideration of various scattering mechanisms:

$$\mu = 22.5 \left[F_{1/2}(\eta) z_l T_K^{1/2} (m^*)^{3/2} \left(\frac{1}{\varepsilon_\hbar} - \frac{1}{\varepsilon_l} \right) \right]^{-1} \times \left(\frac{D_{3/2,3/2}}{D} \right) \tag{32}$$

where $F_{1/2}(\eta)$ represents the half-integral Fermi–Dirac integral and η $(=E_F/k_B T_K)$ is the reduced Fermi energy, T_K is the temperature, z_l $(=\hbar\omega/k_B T_K)$ is the reduced polar optical phonon energy, m^* is the electron effective mass, and ε_l and ε_h are low and high frequency dielectric constants, respectively. $D_{3/2,3/2}$ and D refer to the determinants that contain the variational integrals [197].

This model was used by Makino et al. [195] to understand free carrier mobility in n-type ZnO; the calculation is shown in Fig. 20. The polar optical-phonon scattering mechanism
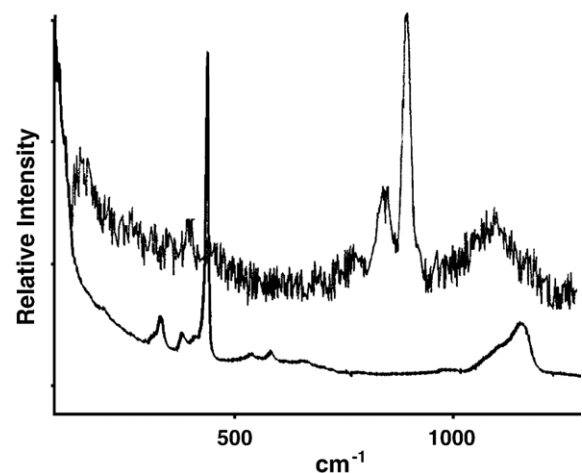

Fig. 19. (Lower trace) Raman spectrum of a 500 nm thick ZnO film deposited on a borosilicate glass substrate indicating vibrational features intrinsic to the crystalline wurtzite phase; (Upper trace) Raman spectrum of the same film after heating for 2 hours in air at 400 °C. ZnO has chemically transformed to zinc borate according to the following equation.

$3\,ZnO\,(film) + 2\,B_2O_3\,(glass\ substrate) = Zn_3B_4O_9$
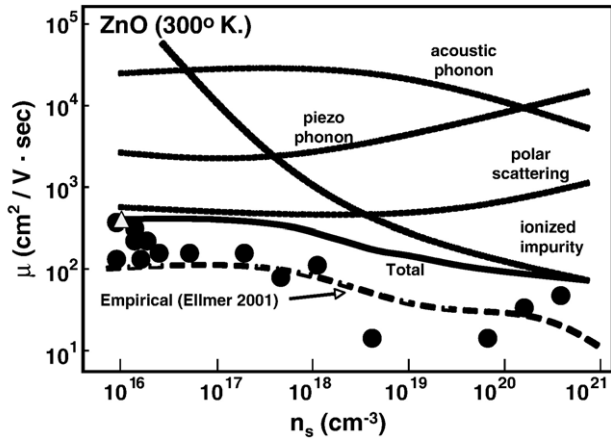
(Ref. [230]).
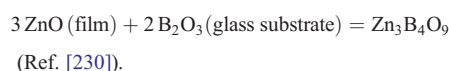
Fig. 20. Comparison of drift mobility calculations (solid curve) with Hall-effect measurements for undoped and doped epitaxial films (filled circles) [54,195]. The thick dashed line is the experimental fit for ZnO [54,198].

dominates when the carrier concentration is less than 10^{17} cm^{-3}, whereas the ionized impurity scattering process is predominant when the carrier concentration is greater than 10^{20} cm^{-3} (again, only in homogeneously doped systems). It is uncertain whether or not a mobility minimum exists when the carrier concentration is in the range from 10^{18} to 10^{19} cm^{-3}; this result was not seen by Ellmer. Nevertheless, Fig. 20 provides a theoretical limit for the electron mobility in donor doped ZnO. It is worth noting that the trend of calculated carrier mobility as a function of free carrier density is similar to that predicted by an empirical formula after Masetti et al. [198]:

$$\mu = \mu_{min} + \frac{\mu_{max} - \mu_{min}}{1 + (n_e/n_{ref1})^{a_I}} - \frac{\mu_1}{1 + (n_{ref2}/n_e)^{a_1}} \qquad (33)$$

where μ_{max} refers the lattice mobility, μ_{min} is the ionized impurity mobility, $\mu_{min} - \mu_1$ represents clustering mobility, n is the concentration, and α is the coefficient [54,198].

The model was developed for doped Si and was used by Ellmer [54] to fit the experimental data of ZnO based oxides, which appears in Fig. 20 as the thick dashed line. Both theoretical and empirical carrier mobility models have been developed for Si or GaAs systems and have been under consideration for several decades. The scattering process continues to stimulate continued investigation in doped metal oxide semiconductors owing to similarities characteristic of traditional free carrier semiconductors like silicon. Caution, however, must be exercised in that both chemical and structural homogeneity is easier to achieve in a material like silicon than in metal oxide systems.

For both of these material systems, however, the universal nature of scattering allows validation of theoretical scattering models through free carrier mobility measurements as a function of dopant concentration and temperature. Recently, enhanced electron mobility was observed in high-quality MBE (Molecular Beam Epitaxy) deposited ZnO thin films grown on a ScAlMgO$_4$ substrate with Mg$_{0.15}$Zn$_{0.85}$O as the buffer layer [199]. The measured mobility, 440 cm^2/Vs, is nearly identical with that predicted from the theoretical calculation, shown in

Fig. 20 as the triangular symbol. The efficacy of this model to predict carrier mobilities in pristine ZnO films with higher carrier densities still remains to be tested. Validation of the model in this regime is only possible for carefully grown ZnO films.

4.2. Enhanced electron mobility in TCO films

The underlying challenge posed by this discussion relates to how the mobility can be increased in TCO films so as to approach the theoretical limits? During the past two decades, some progress has been evident in reducing the resistivity of TCO films (as shown in Fig. 18), resulting partially from improvements in fabrication techniques and better attention to chemical composition and resident impurities. While larger dopant concentrations lead to higher free carrier densities, care must be exercised so that the solubility limit of the dopant is not exceeded resulting in phase separation or transformation of the crystal structure. Moreover, it is not desirable for TCO films to have too high a carrier concentration ($>10 \times 10^{20}$ cm^{-3}) because of potential free carrier absorption in the near-infrared range, which is a detrimental factor in many applications (such as solar cells) requiring a wide optical bandpass from 400 to 1100 nm. Optimization of dopant concentration has been successful in reducing film resistivity to the 10^{-4} Ω cm range. Further reduction in resistivity to 10^{-5} Ω cm [120,123,124,200,201] necessitates improvement in free carrier mobility if the carrier concentration has been pushed to the limit (Table 1).

Two approaches can be considered as a means to increase carrier mobility: (1) controlling the density of resident defects in order to reduce ionized impurity scattering; and (2), tailoring the nano/microstructure to reduce the grain boundary scattering. Indeed, Hall mobility was improved by an order of magnitude in rf-sputtered ZnO:Al thin films by changing the target chemistry [202]. In spray pyrolyzed ITO films, post annealing in hydrogen increased the mobility by a factor of three to 150 cm^2/Vs [203]. A very high conductivity (~22,700 S/cm) was observed in ITO films produced by means of e-beam evaporation with zone-confined improvement [204] — tailoring the dopant segregation at grain boundaries to enhance the mobility (up to 10^3 cm^2/

Table 1
Current TCO's with resistivities below 1.6×10^{-4} Ω cm

Composition	Method	μ (cm^2/Vs)	ρ ($\times 10^{-4}$ Ω cm)	Ref
Al:ZnO	PLD	47.6	0.85	[124]
Al:ZnO	Sputtering	28.2	1.39	[97]
ITO	PLD		0.95	[120]
ITO	rf magnetron sputtering		1.2	[79]
Mo:In$_2$O$_3$	Sputtering	80	1.6	[73] With: Ti, Ta, Zr, Nb, and W
ITO	Solution/Ag as the 2nd phase		0.82	[157]
ITO	Spray		0.77	[167]
ITO	Nanowires		0.629	[201]
Mo:In$_2$O$_3$	rf magnetron sputtering	94	1.5	[72]

Vs). Selective doping was carried out on this material by using transition metal elements deeper in the periodic table such as molybdenum. Introduction of such d-state metal dopants into the structure was predicted to not only improve mobility but also reduce optical absorption. The d-states of Mo do not hybridize with the s-states of In [27]. Hence, the resulting dispersion associated with the conduction band after Mo doping remains similar to that seen in pure indium oxide suggesting a similar effective mass in the doped system. The doped material has been defined as a magnetically mediated TCO [27].

Knowledge of the temperature dependence of free carrier mobilities also is critical to identifying the predominant scattering mechanism. The mobility associated with ionized impurity scattering in high charge carrier concentration (degenerate) semiconductors is independent of temperature while the mobility associated with thermal lattice vibration scattering is inversely proportional to the temperature. The Hall measurements on ITO and SnO_2:F films deposited using different methods lends support to this analysis [205].

The role of nano/microstructure on Hall mobility is much more complex than expected. In polycrystalline films that contain relatively large grains, carrier scattering was found to be dominated by ionized impurity scattering at low temperature and phonon scattering at high temperature, provided that the carrier concentration was in excess of 5×10^{18}/cm^3 [205]. Hence, grain boundary effects were found to be negligible. In TCO thin films, the resistivity often is observed to be thickness dependent, which is generally related to the level of crystallinity in the film that appears in x-ray diffraction patterns as line broadening. Anomalous values of mobility are expected if the crystallite size is on the order of or less than the electron mean free path (Eq. (9)) [206]. Improvement of film crystallinity and grain size uniformity has been shown to be effective at increasing Hall mobility. In addition, carrier scattering from the planar imperfections of the crystals, primarily at grain boundaries is a crucial factor in controlling the mobility in polycrystalline films. Low angle grain boundaries also may be found in epitaxial films [88] and, for example, have been found to reduce carrier mobility in ZnO:Al films.

Scattering from grain boundaries involves two primary mechanisms, which exist in nearly all TCO films, including epitaxial deposited films [88]. However, the scattering process is difficult to quantitatively analyze: (1) ionized impurities can reduce the grain boundary potential, thus decreasing the barrier height for charge transfer, which results in high electron mobility; and (2), large grain boundary angles and resident defects and segregation phases in the grain boundaries will increase carrier scattering and therefore reduce electron mobility. Since grain boundary scattering is deleterious to carrier mobility in polycrystalline films, the absence of these microscopic interfaces in amorphous films may suggest a path forward to a significant improvement in carrier mobility. This is an approach currently undertaken by a number of research groups. Improved mobility in amorphous TCO materials has been realized and theoretically explained in $2CdO \cdot GeO_2$ thin films [192], where the presence of overlapping Cd 5s orbitals provides continuous carrier conduction pathways that are not impeded by the presence of grain boundaries. The challenge, here, is to develop amorphous compositions of polycrystalline TCO materials, many of which, by themselves, are not amenable to forming an amorphous phase. There are two prerequisite conditions for achieving amorphous TCO films: (1) the existence of a disordered network; and (2), the materials must be TCO in the analogous crystalline form. The case of CdO will be discussed below.

Since doped CdO has shown unprecedented conductivity and mobility, primarily by researchers at Northwestern University [23,143,207–209], this material warrants special consideration. Yan et al. deposited 2.5 at.% Sn doped CdO thin films by means of a PLD method and observed conductivity as high as 42,000 S/cm (resistivity $\sim 2.4 \times 10^{-5}$ Ω cm) and mobility (609 cm^2/Vs). To this point in time, this material holds the record for the lowest resistivity and highest mobility in a TCO film [208]. The mobility had a strong dependence on the nature of the substrate with measured values of 609, 330, and 27 cm^2/Vs for MgO (111), MgO (100), and Corning 1737 glass, respectively. The nature of the substrate affected film orientation, morphology, and crystallinity, and thereby, influenced the electron mobility. This was also shown in more recent work by this group for Y:CdO films in Fig. 21, where correlations among optical response, carrier mobility, and resident microstructure can be seen. After this work, MOCVD [23,143] was used to grow In:CdO thin films on glass, which exhibited a mobility of about 70 cm^2/Vs [23] for a doping level between 2% and 7%; the conductivity reached 10,000 S/cm at a dopant concentration of 5 at.% In [23]. Again, a high mobility was observed, ~ 125 cm^2/Vs for the 2.5 at.% In doped CdO film on an MgO (100) substrate. Undoped CdO has a band gap of about 2.4 eV, which broadens upon addition of donor dopants due to the Burstein–Moss shift; $E_g \sim 3.1$ eV in 5 mol.% In doped CdO [207]. Band structure calculations of In doped CdO revealed the presence of hybridization between the 5s-orbitals of both metal cations, resulting in a uniform charge density distribution. Hence, the high dispersion associated with the CBM of undoped CdO persists after doping which drives the high mobility.

Based upon this discussion, several general guidelines for developing materials with increased mobility follow. To achieve TCO film resistivities below 10^{-4} Ω cm with free carrier densities on the order of 10×10^{20} cm^{-3}, the electron mobility must be greater than 62.5 cm^2/Vs. Suggested approaches to achieve this metric are listed below.

(1) With respect to dopant, appropriate transition metal cations with d-states close in energy to the matrix oxide metal cation may improve electron mobility, provided that the dopant is homogenously distributed throughout the dielectric.

(2) In terms of film growth, effective improvement of carrier mobility will be achieved through control of resident defects and the attendant nano/microstructure during growth (*in situ*) rather than by invoking post deposition processing (e.g. annealing) (*ex situ*). *In situ* annealing at an appropriate temperature and oxygen activity will likely
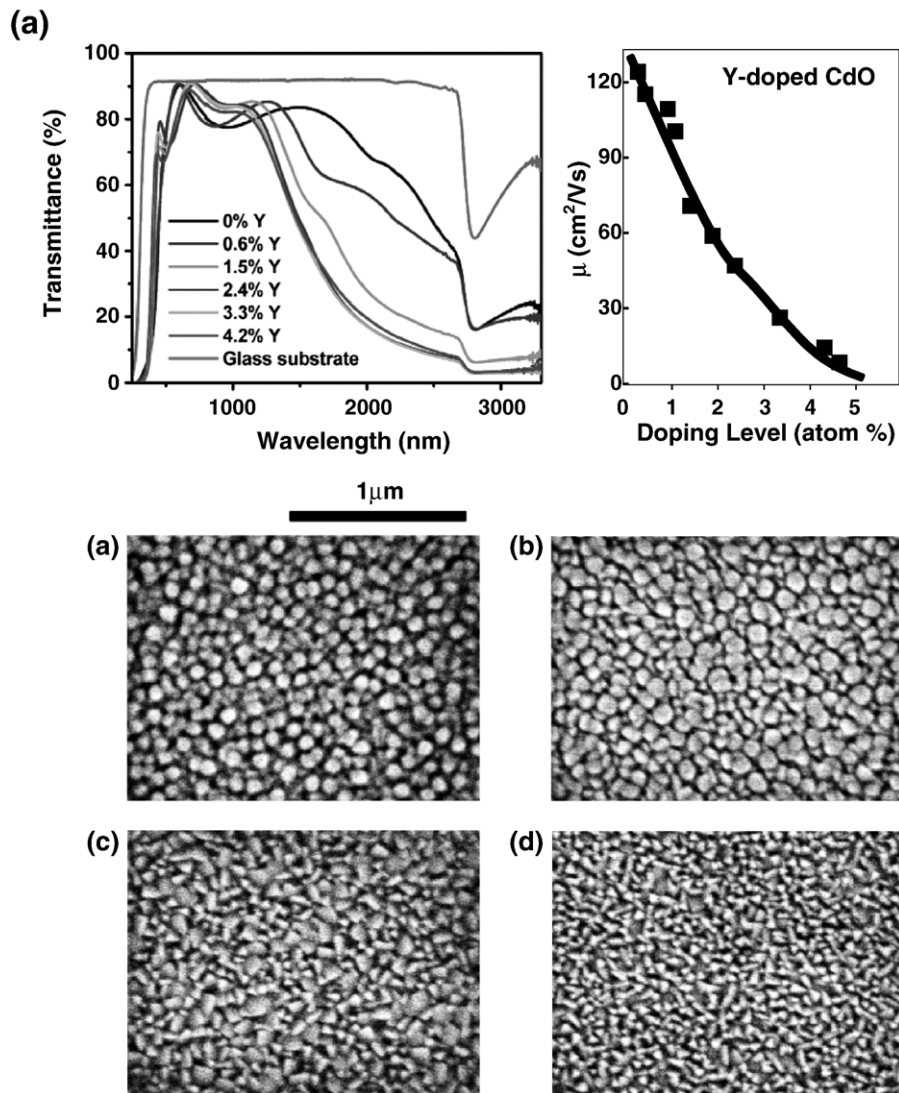
Fig. 21. Correlation of optical response (top left), carrier mobility (top right), and microstructure (above) as a function of dopant concentration in yttrium-doped CdO films. Micrographs (A)–(D) correspond to 0.6%, 1.5%, 2.4%, and 4.2% dopant atomic composition respectively (taken from Ref. [23].).

minimize disorder in the crystalline lattice; in particular, point defects and dislocations, can be reduced during layer by layer growth, rather than being removed by post-deposition annealing.

(3) Attempts to move toward theoretical limits of electron mobility necessitate careful experimental investigations on the dependence of local chemical homogeneity, grain orientation, residual stress within the films, and grain size, which play crucial roles in controlling the characteristics of the attendant band structure, such as band dispersion, band gap, and band overlap.

(4) Theories that apply to conventional semiconductors can provide a fundamental basis to understand carrier scattering mechanisms in metal oxide systems, from which a more precise foundation can be developed by considering non-stoichiometry and nano/microstructure.

(5) In addition to knowledge of the calculated band structures of TCO films, a more rigorous theoretical understanding

is needed to quantitatively investigate the role of grain size and grain boundary influence on scattering.

5. Future directions in TCO research

Design and synthesis of materials that are simultaneously transparent and conducting continue to be challenging requiring innovative approaches to achieve better performance for prospective device applications. A growing ability to manipulate materials structure and chemistry at the nanoscale affords the opportunity to pursue new directions in the development of these materials. Three avenues that require further attention are summarized in this section. The first involves hydrogen doping of certain metal oxides. This process can promote formation of shallow donors leading to a marked increase in conductivity. The structural implications associated with the use of different processing approaches to incorporate these interstitial impurities remain to be understood. A second direction involves

continued investigation of the electride materials described earlier in this review. These supramolecular oxide materials with interconnected cage-like structures promote conductivity by means of a mechanism whereby weakly bound electrons serve the role of anions in the structure in order to balance charge. A third avenue to pursue focuses on the development of tunnel barrier materials that are based upon imposing impedance matching conditions at interfaces. Such materials will theoretically support optical transmission through thin metal film/dielectric multilayer structuress and through nano-architectured interfaces. Included here are the plasmonic meta-materials which are periodic architectured arrays that can show high transmission, again by impedance matching to the ambient environment.

5.1. Hydrogen impurities in oxides

It is well-known that when metal oxides or doped metal oxides are subjected to reducing environments (e.g., hydrogen) at elevated temperatures or in an electrochemical cell, a conducting and transparent phase of the material can result [210,211]. At temperatures of about 400 °C, hydrogen dissociatively adsorbs onto these oxide surfaces and the resulting atomic hydrogen becomes available to reduce either matrix or dopant metal cations providing free carriers in defect levels lying near the conduction band minimum as a result of oxygen vacancy formation through release of water. However, if hydrogen is incorporated interstitially into certain metal oxide films under conditions where reduction does not occur, first principles band energy calculations suggest that it alone can act as a shallow donor to induce *n*-type conductivity [212,213]. Fig. 22 summarizes results of recent electron band structure calculations where the hydrogen donor pinning level has been identified for several metal oxides.

ZnO containing hydrogen impurities has been formed by annealing bulk crystals in hydrogen in a closed tube [214,215], by means of sputter deposition in a hydrogen ambient [216,217], by subjecting samples to a hydrogen plasma [218], and by ion beam irradiation. In all cases, *n*-type conducting
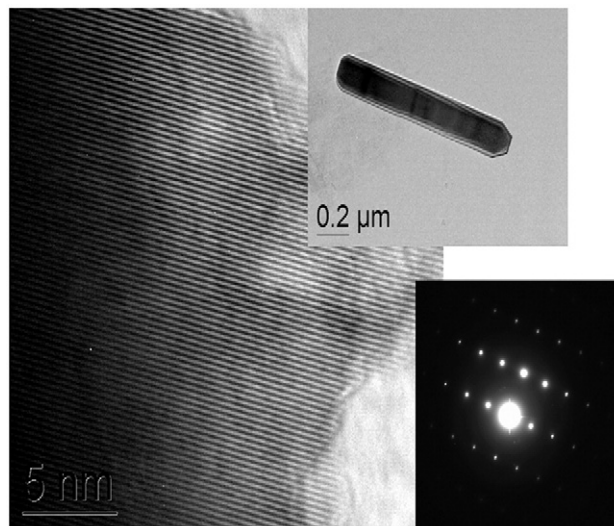
Fig. 23. TEM of a crystalline ZnO nanorod formed by a solution templating route. A selected area diffraction patters appears as an inset in the figure and confirms the wurtzite phase (unpublished data from PNNL).

ZnO was formed. Low temperature infrared measurements of an annealed single crystal sample revealed presence of a strong mode at about 3326 cm^{-1} that has been assigned to an –OH stretching vibration where the hydrogen exists in an anti-bonding configuration relative to the c-axis of the crystal. Related work reported Hall measurements on ZnO crystals and epitaxial films treated in a hydrogen plasma that confirmed the *n*-type nature of the induced conductivity [219]. Other methods for incorporating hydrogen in metal oxides can include ion implantation, magnetron sputtering using hydrogen as the sputter gas, and MOCVD approaches. Studies referenced here provide experimental evidence of incipient hydrogen in ZnO that promotes *n*-type conductivity.

The method by which hydrogen is incorporated into oxide lattices may indeed induce contrasting structural perturbations. Further development of structure-property relationships in these systems is a continuing area of interest. The nature and distribution of interstitial hydrogen in ZnO is still a matter of contention particularly in lieu of reports that claim stability of a hydrogen–oxygen complex in hydrothermally derived ZnO at temperatures near 1000 °C. Recent work in this laboratory has applied solid-state magnetic resonance methods to probe localized hydrogen sites in ZnO nanorods, specie distributions, and transport dynamics in these hydrothermally derived materials [220,221]. A TEM (Transmission Electron Microscopy) image and selected area diffraction pattern for high aspect ratio ZnO nanorods is shown in Fig. 23. The ability to distinguish localized hydrogen sites not only strongly and weakly bound to the surface but also intrinsic to the nanotubes is key to understanding how the defect structure controls properties. The NMR (Nuclear Magnetic Resonance) spectrum obtained from these nanorods contrasts starkly with spectra of micrometer size powder samples of ZnO and Zn(OH)$_2$. Proton resonance lines persist following high temperature annealing indicating presence of a tightly bound species as can be seen in
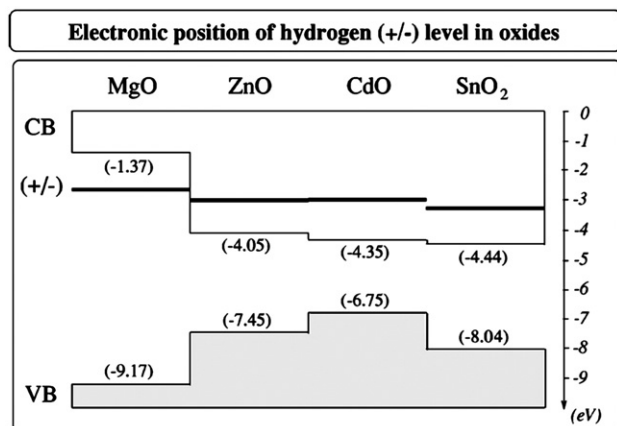

Fig. 22. Position of the hydrogen pinning level (thick lines) in several oxides. The CBM and VBM band edge energies appear in parentheses (figure taken from Ref. [212]).

Fig. 24. Future directions in this work will also likely focus on studies of oriented ZnO nanorod films to better understand the role of resident anisotropy on conductivity pathways and the influence of conductivity anisotropy on optical properties.

5.2. Oxide-based electrides

A previous section in this paper discussed the remarkable properties of a ceramic oxide material constructed of interconnected cages. The complex oxide $12CaO–7Al_2O_3$ (known as C12A7) can be converted from a transparent insulator to an electrical conductor through UV irradiation of the material into which hydride ion (H^-) had been incorporated. The light-induced charge separation that ensues, creates a weakly bound *localized electron* that can execute thermally-induced hopping between available sites (cages) thereby promoting conductivity. However, irradiation also leads to a coloration and associated absorption of the material that is found to increase with conductivity. Previous work suggests the existence of deep electron trap states corresponding to absorption in the near IR and UV spectral regions. These transitions, associated with both intercage and intracage transitions, determine the region of transparency of the material [222].

The grand challenge for TCO materials, as stated in the introduction of this paper, is to decouple the absorptive properties of the material from the attendant conductivity. Several routes to attack this challenge for oxide electrides can be envisioned from published modeling studies of this system [223,224]. Fig. 25 shows marked changes in the electronic band structure when the irradiated conducting material is compared with the neat starting material. Additional insight to engineering ceramic oxide structures with porous interconnectivity also can be inferred from reference to zeolite systems that include both alkali aluminosilicates and aluminophosphates. For example, the effect of cage size (which can be altered by substitution of different cation oxides in the structure) on the optical absorption spectrum of the conducting phase would be of interest.

5.3. Impedance matching designs

Up to this point, this review has considered oxide-based materials that are initially transparent but also non-conducting. Chemical modification to such materials is then invoked to subsequently induce conductivity. In some instances (electrides and polaron conductors) the material may indeed show undesirable absorption at visible wavelengths necessitating further modification to mitigate the issue. Alternate contrasting approaches are under investigation for improving the visible transmittance of what are normally opaque materials that may already be conducting. These methods are based upon impedance matching of the dielectric response of the material to the ambient environment. Two approaches to improve transparency of conducting materials are discussed below. They focus on designing multilayer structures that promote tunneling through a barrier (conducting metal film), and designing structurally tailored morphologies (meta-materials) [225] that promote the targeted optical response.

A frustrated total internal reflection experiment was carried out to show that an appropriate sandwich structure, comprised of a thin metal layer sandwiched between two high index dielectric layers, can indeed pass visible light [226]. In this case 217 nm thick ZnS films served as high index dielectric layers in contact with a 40.3 nm thick conducting silver film. A transmission window opened in the visible region of the spectrum, centered near 600 nm. In the absence of the dielectric, only a small amount of light was transmitted by the metal film alone. The multilayer geometry was used recently to improve the transparency of a TCO material. The designed multilayer was comprised of a high index ITO film, a metal film (Ag–Ti alloy), and a second ITO layer [227]. An optimum transmittance of 94% was realized with only a small increase in resistivity when compared with ITO alone. The presence of the metal alloy layer also promoted higher thermal stability and durability particularly in humid environments.

A second approach for enhancing transmission requires forming sub-wavelength hole arrays in a thin film. This has first been exploited for metal films at near infrared wavelengths
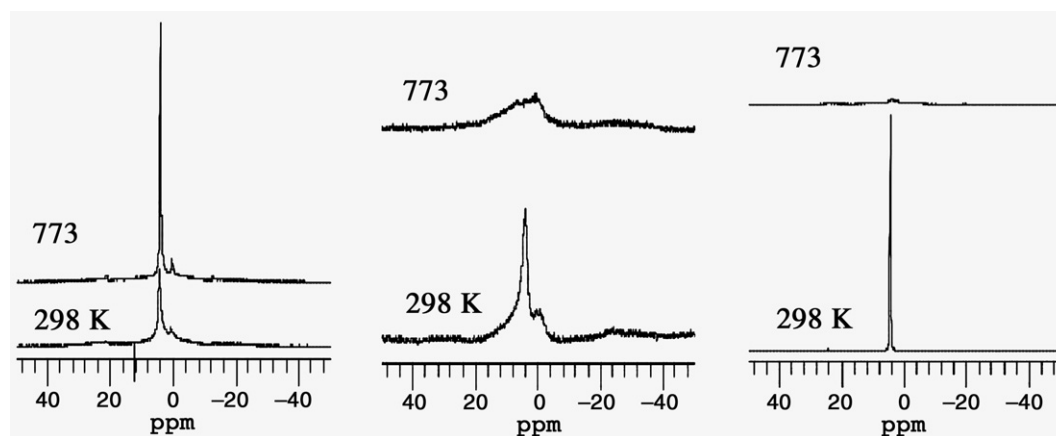

Fig. 24. ^1H NMR spectra of solution derived ZnO nanorods (left), micrometer size ZnO powder from Aldrich (center), and $Zn(OH)_2$ powder supplied by Aldrich measured at room temperature and following subsequent heating to 773 K. The nanorods securely bind hydrogen at high temperature suggesting a tightly bound hydrogen complex in the matrix. The conducting properties of these materials are currently under investigation at PNNL.
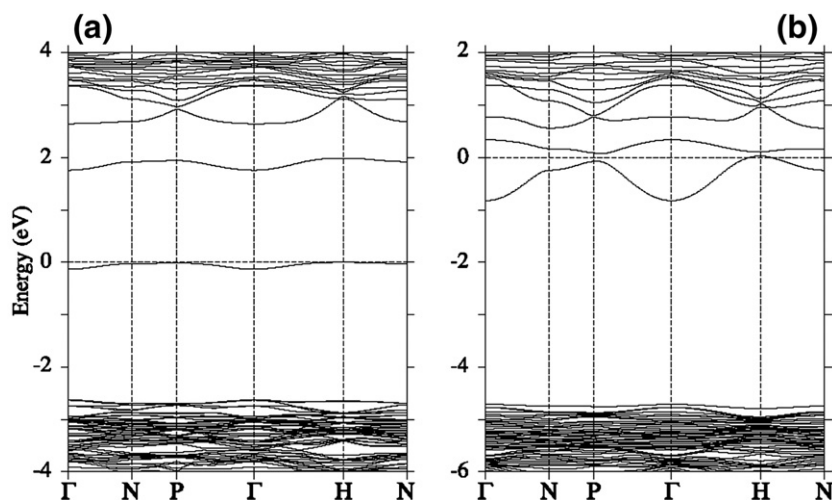
Fig. 25. Electron energy band structure of C12A7 that has been substituted with hydride ion before (a) and after (b) UV irradiation to induce a persistent conducting state. Results show the formation of a hybrid *defect* band within the bandgap of the material. Results also suggest that any increase in the density of states in this band (favoring higher conductivity) would also increase absorption of light thereby reducing optical transmission (figure taken from Ref. [28]).

[228]. In this early work, the transmittance through a 200 nm diameter thick silver film could be markedly enhanced. Here, a focused ion beam created an array of cylindrical holes in the film that was supported on a glass substrate. Hole diameter, spacing, and density comprised the critical parameters that controlled transmission through the film and its angular dependence. The concept was recently pushed to shorter wavelengths in the visible region of the spectrum [229]. Here, structured metal films were shown to have very high transmissivity over certain wavelength regions that depend upon the dielectric constant of the film material and the surrounding medium. Microstructure densities on the order of 20% were associated with the highest transmittance. Concepts discussed in these articles may impact future design of TCO films resulting in both improved transmittance and conductivity.

6. Conclusions

Cumulative success in understanding rudimentary structure–property relationships in transparent conducting oxides has been demonstrated. However, additional challenges abound for achieving materials with even higher conductivity and transparency over extended wavelength ranges. At this point in time innovative processing approaches have been developed that allow free carriers to be incorporated into oxide systems in a controlled manner. We also have become aware of the critical materials parameters that restrict the density of defect states and hence the number of free carriers that can be introduced both for *n*-type and *p*-type materials. However, our understanding of carrier mobility mechanisms and approaches to enhance mobility lags and demands increased attention. For example, structured films of the same composition, even those deposited epitaxially, show marked variations in mobility. In polycrystalline materials, this is presumably caused by variations in charge transport within the grain itself, on the surface (grain boundary), and across grain boundaries. Factors that induce composition

variations at grain boundaries, particularly for indium-containing compositions, are necessary to understand since this will necessarily impact charge transport. To negate this issue, recent research has focused on amorphous phase materials. While the grain boundary problem is significantly simplified, the issue of film substrate interactions that can act to alter film chemistry and mobility now demands increased attention [230].

Understanding conductivity mechanisms based upon weakly bound charge carrier hopping among available sites are critical to further improvement of electride and polaron conductors which seem to offer a new route to TCO materials. Methods for further reducing weak optical absorption in the visible region of the spectrum while maintaining conductivity are of keen interest. Manipulation of cage size and variation of cage constituent atoms seem likely avenues to pursue. This is an area where electronic structure modeling studies can effectively guide the design of new materials.

A final area that holds promise for improving TCO properties involves structural manipulation on the nanometer scale. The recent work on making metals transparent may have some application to these TCO materials. Furthermore, deposition of oxide films with structural anisotropy would appear to offer yet another approach to properties improvement. Oriented nanotubes may indeed exhibit anisotropic optical properties that are decoupled from film conductivity. These tailored interface approaches are under current investigation and likely will lead to a cadre of improved next generation materials.

Finally, much of the fundamental materials research in this area is being driven by applications from both commercial and military venues. Perhaps one of the most successful applications of TCO's involves low-emissivity coatings for windows where the plasma wavelength of the coating can be designed to either pass near infrared wavelengths from sunlight (cold climates) or reject near IR wavelengths (hot climates). Developments of active windows for achieving this duality in a single window are under consideration. Heat reflecting coatings for ovens,

coatings to dissipate static (copy machine glass plates, touch-panel controls, and electromagnetic shielding) comprise additional consumer product applications that demand better materials. Major markets in the solar cell, flat-panel display, and solid-state lighting areas also require development of improved TCO materials with increased robustness and resistance to changes in optoelectronic properties. In addition to these several important applications that will impact consumer products, the conundrum of building a material that is both conducting and transparent will drive our curiosity to further develop approaches that lead to decoupling these variables.

Acknowledgements

References

[1] K. Badeker, Ann. Phys. (Berlin) 22/4 (1907) 749.
[2] K.L. Chopra, S. Major, D.K. Pandya, Thin Solid Films 102/1 (1983) 1.
[3] H. Hosono, T. Kamiya, M. Hirano, Bull. Chem. Soc. Jpn. 79/1 (2006) 1.
[4] H. Kawazoe, K. Ueda, J. Am. Ceram. Soc. 82/12 (1999) 3330.
[5] T. Minami, Semicond. Sci. Technol. 20/4 (2005) S35.
[6] D.S. Ginley, J.D. Perkins, H. Kawazoe, D.M. Newns, A.B. Kozyrev, Proceedings of the Materials Research Society, Materials Research Society, 2001, p. 433.
[7] D.C. Paine, H.-Y. Yeom, B. Yaglioglu, in: G.P. Crawford (Ed.), Flexible Flat Panel Displays, Wiley Interscience, John Wiley and Sons, 2005, p. 79.
[8] A.N. Banerjee, K.K. Chattopadhyay, Prog. Cryst. Growth Charact. Mater. 50/1-3 (2005) 52.
[9] R. Kykyneshi, B.C. Nielsen, J. Tate, J. Li, A.W. Sleight, J. Appl. Phys. 96/11 (2004) 6188.
[10] D. Emin, in: C.L. Chien, C.R. Westgate (Eds.), The Hall Effect and Its Applications, Plenum Publishing, New York, 1980, p. 281.
[11] D. Bertho, C. Jouanin, Phys. Rev., B 35/2 (1987) 626.
[12] D. Bott, Phys. Technol. 16/3 (1985) 121.
[13] L.P. Yu, M. Chen, L.R. Dalton, Chem. Mater. 2/6 (1990) 649.
[14] C.F. Windisch, G.J. Exarhos, K.F. Ferris, M.H. Engelhard, D.C. Stewart, Thin Solid Films 398 (2001) 45.
[15] R.R. Owings, G.J. Exarhos, C.F. Windisch, P.H. Holloway, J.G. Wen, Thin Solid Films 483/1-2 (2005) 175.
[16] D.S. Ginley, C. Bright, MRS Bull. 25/8 (2000) 15.
[17] The 1st International Symposium on Transparent Conducting Oxide, IESL-FORTH, Crete, Greece, 2006, http://www.certh.gr/65278BEC.en.aspx.
[18] R.G. Gordon, MRS Bull. 25/8 (2000) 52.
[19] J.M. Ziman, Principles of the Theory of Solids, Cambridge University Press, 1972.
[20] A. Zunger, Defects in Photovoltaic Materials and the Origin of Failure to Dope Them, NREL/CP-590-31034, 2001.
[21] C.F. Windisch, G.J. Exarhos, J. Vac. Sci. Technol. A, Vac. Surf. Films 18/4 (2000) 1677.
[22] E. Burstein, Phys. Rev. 93/3 (1954) 632.
[23] Y. Yang, S. Jin, J.E. Medvedeva, J.R. Ireland, A.W. Metz, J. Ni, M.C. Hersam, A.J. Freeman, T.J. Marks, J. Am. Chem. Soc. 127/24 (2005) 8796.
[24] H. Hosono, M. Yasukawa, H. Kawazoe, J. Non-Cryst. Solids 203 (1996) 334.
[25] M. Orita, H. Ohta, M. Hirano, S. Narushima, H. Hosono, Philos. Mag., B, Phys. Condens. Matter, Stat. Mech. Electron. Opt. Magn. Prop. 81/5 (2001) 501.
[26] C. Persson, Y.J. Zhao, S. Lany, A. Zunger, Phys. Rev., B 72/3 (2005) 035211.
[27] J.E. Medvedeva, Phys. Rev. Lett. 97/8 (2006) 086401.
[28] J.E. Medvedeva, A.J. Freeman, Europhys. Lett. 69/4 (2005) 583.
[29] H.Q. Chiang, J.F. Wager, R.L. Hoffman, J. Jeong, D.A. Keszler, Appl. Phys. Lett. 86/1 (2005) 013503.
[30] M.J. Wagner, R.H. Huang, J.L. Dye, J. Phys. Chem. 97/16 (1993) 3982.
[31] M.J. Wagner, R.H. Huang, J.L. Eglin, J.L. Dye, Nature 368/6473 (1994) 726.
[32] J.E. Hendrickson, W.P. Pratt, R.C. Phillips, J.L. Dye, J. Phys. Chem., B 102/20 (1998) 3917.
[33] K. Hayashi, S. Matsuishi, T. Kamiya, M. Hirano, H. Hosono, Nature 419/6906 (2002) 462.
[34] P.V. Sushko, A.L. Shluger, K. Hayashi, M. Hirano, H. Hosono, Phys. Rev., B 73/1 (2006) 014101.
[35] M. Miyakawa, Y. Toda, K. Hayashi, M. Hirano, T. Kamiya, N. Matsunami, H. Hosono, J. Appl. Phys. 97/2 (2005) 023510.
[36] J.B. Goodenough, Rep. Prog. Phys. 67 (2004) 1915.
[37] J.C. Dyre, T.B. Schroder, Phys. Rev., B 54/21 (1996) 14884.
[38] D. Emin, C.H. Seager, R.K. Quinn, Phys. Rev. Lett. 28/13 (1972) 813.
[39] Y.N. Gartstein, E.M. Conwell, Phys. Rev., B 51/11 (1995) 6947.
[40] K. Kuriyama, Phys. Rev., B 47/19 (1993) 12415.
[41] B.H. Zhang, T. Katsura, A. Shatskiy, T. Matsuzaki, X.P. Wu, Phys. Rev., B 73/13 (2006) 134104.
[42] L.D. Kadam, P.S. Patil, Mater. Chem. Phys. 68/1-3 (2001) 225.
[43] R.R. Owings, P.H. Holloway, G.J. Exarhos, C.F. Windisch, Surf. Interface Anal. 37/4 (2005) 424.
[44] C.F. Windisch, K.F. Ferris, G.J. Exarhos, J. Vac. Sci. Technol. A, Vac. Surf. Films 19/4 (2001) 1647.
[45] N.W. Grimes, Phys. Technol. 6 (1975) 22.
[46] C.F. Windisch, G.J. Exarhos, R.R. Owings, J. Appl. Phys. 95/10 (2004) 5435.
[47] C.F. Windisch, K.F. Ferris, G.J. Exarhos, S.K. Sharma, Thin Solid Films 420 (2002) 89.
[48] S. Goodwin-Jahansson, P.H. Holloway, G. McGuire, B.L. Cozzens, R. Schwartz, G.J. Exarhos, Proc. SPIE 3987-32:225, 2000.
[49] D. Attygalle, W.B.J. Ingler, X. Deng, ECS 210th Meeting Abstract: Abstract, vol. 1554, 2001.
[50] A.J. Freeman, K.R. Poeppelmeier, T.O. Mason, R.P.H. Chang, T.J. Marks, Mrs Bull. 25/8 (2000) 45.
[51] C.G. Granqvist, A. Hultaker, Thin Solid Films 411/1 (2002) 1.
[52] M. Kemell, M. Ritala, M. Leskela, Crit. Rev. Solid State Mater. Sci. 30/1 (2005) 1.
[53] M. Batzill, U. Diebold, Prog. Surf. Sci. 79/2-4 (2005) 47.
[54] K. Ellmer, J. Phys. D: Appl. Phys. 34/21 (2001) 3097.
[55] S. Sheng, G.J. Fang, C. Li, S. Xu, X.Z. Zhao, Phys. Status Solidi, A Appl. Res. 203/8 (2006) 1891.
[56] H. Kawazoe, M. Yasukawa, H. Hyodo, M. Kurita, H. Yanagi, H. Hosono, Nature 389/6654 (1997) 939.
[57] H. Kawazoe, H. Yanagi, K. Ueda, H. Hosono, MRS Bull. 25/8 (2000) 28.
[58] M.A. Marquardt, N.A. Ashmore, D.P. Cann, Thin Solid Films 496/1 (2006) 146.
[59] K. Ramamoorthy, K. Kumar, R. Chandramohan, K. Sankaranarayanan, R. Saravanan, I.V. Kityk, P. Ramasamy, Opt. Commun. 262/1 (2006) 91.
[60] U. Ozgur, Y.I. Alivov, C. Liu, A. Teke, M.A. Reshchikov, S. Dogan, V. Avrutin, S.J. Cho, H. Morkoc, J. Appl. Phys. 98/4 (2005) 041301.

[61] P.F. Carcia, R.S. McLean, M.H. Reilly, Z.G. Li, L.J. Pillione, R.F. Messier, J. Vac. Sci. Technol. A, Vac. Surf. Films 21/3 (2003) 745.

[62] N.L. Dehuff, E.S. Kettenring, D. Hong, H.Q. Chiang, J.F. Wager, R.L. Hoffman, C.H. Park, D.A. Keszler, J. Appl. Phys. 97/6 (2005) 064505.

[63] K.B. Sundaram, A. Khan, J. Vac. Sci. Technol. A, Vac. Surf. Films 15/2 (1997) 428.

[64] K. Yim, C. Lee, Cryst. Res. Technol. 41/12 (2006) 1198.

[65] S. Rossnagel, in: W. Sproul, K. Legg (Eds.), Opportunities for Innovation: Advanced Surf. Eng. Technomic Publishing Co., Switzerland, 1995.

[66] P.J. Kelly, R.D. Arnell, Vacuum 56/3 (2000) 159.

[67] P.J. Kelly, J. Hisek, Y. Zhou, R.D. Pilkington, R.D. Arnell, Surf. Eng. 20/3 (2004) 157.

[68] P.J. Kelly, J. O'Brien, R.D. Arnell, Vacuum 74/1 (2004) 1.

[69] E.M. Alkoy, P.J. Kelly, Vacuum 79/3-4 (2005) 221.

[70] M.S. Hwang, H.J. Lee, H.S. Jeong, Y.W. Seo, S.J. Kwon, Surf. Coat. Technol. 171/1-3 (2003) 29.

[71] Y. Yoshida, T.A. Gessert, C.L. Perkins, T.J. Coutts, J. Vac. Sci. Technol. A, Vac. Surf. Films 21/4 (2003) 1092.

[72] N. Yamada, T. Tatejima, H. Ishizaki, T. Nakada, Jpn. J. Appl. Phys. Part 2, Lett. Express Lett. 45/42-45 (2006) L1179.

[73] A.E. Delahoy, S.Y. Guo, J. Vac. Sci. Technol. A, Vac. Surf. Films 23/4 (2005) 1215.

[74] C.H. Jeong, J.T. Lim, J.H. Lee, M.S. Kim, J.W. Bae, G.Y. Yeom, Jpn. J. Appl. Phys., Part 1 Regul. Pap. Brief Commun. Rev. Pap. 45/10B (2006) 8457.

[75] H.C. Lee, O.O. Park, Vacuum 80/8 (2006) 880.

[76] H.C. Lee, J.Y. Seo, Y.W. Choi, D.W. Lee, Vacuum 72/3 (2003) 269.

[77] Y.S. Kim, Y.C. Park, S.G. Ansari, J.Y. Lee, B.S. Lee, H.S. Shin, Surf. Coat. Technol. 173/2-3 (2003) 299.

[78] D. Kim, J. Non-Cryst. Solids 331/1-3 (2003) 41.

[79] R. Das, S. Ray, Jpn. J. Appl. Phys., Part 1 Regul. Pap. Short Notes Rev. Pap. 44/3 (2005) 1367.

[80] J.M. Park, J.S. Hong, J.Y. Yang, J.J. Kim, S.H. Park, H.M. Kim, J.S. Ahn, J. Korean Phys. Soc. 48/6 (2006) 1530.

[81] Y.S. Jung, H.Y. Seo, D.W. Lee, D.Y. Jeon, Thin Solid Films 445/1 (2003) 63.

[82] R. Das, S. Ray, J. Phys. D: Appl. Phys. 36/2 (2003) 152.

[83] H.Y. Yeom, N. Popovich, E. Chason, D.C. Paine, Thin Solid Films 411/1 (2002) 17.

[84] T. Tohsophon, N. Sirikulrat, Sol. Energy Mater. Sol. Cells 90/18-19 (2006) 3444.

[85] T. Minami, T. Miyata, Y. Ohtani, Y. Mochizuki, Jpn. J. Appl. Phys., Part 2 Lett. Express Lett. 45/12-16 (2006) L409.

[86] J.G. Lu, Z.Z. Ye, Y.J. Zeng, L.P. Zhu, L. Wang, J. Yuan, B.H. Zhao, Q.L. Liang, J. Appl. Phys. 100/7 (2006) 073714.

[87] X.T. Hao, L.W. Tan, K.S. Ong, F.R. Zhu, J. Cryst. Growth 287/1 (2006) 44.

[88] K. Ellmer, G. Vollweiler, Thin Solid Films 496/1 (2006) 104.

[89] S.S. Lin, J.L. Huang, P. Sajgalik, Surf. Coat. Technol. 190/1 (2005) 39.

[90] B.G. Choi, I.H. Kim, D.H. Kim, K.S. Lee, T.S. Lee, B. Cheong, Y.J. Baik, W.M. Kim, J. Eur. Ceram. Soc. 25/12 (2005) 2161.

[91] R. Das, S. Ray, Indian J. Phys. 78/9 (2004) 901.

[92] J. Ma, X.T. Hao, S.Y. Zhang, H.L. Ma, J. Mater. Sci. Technol. 19/4 (2003) 363.

[93] D. Herrmann, M. Oertel, R. Menner, M. Powalla, Surf. Coat. Technol. 174 (2003) 229.

[94] C. Agashe, O. Kluth, G. Schope, H. Siekmann, J. Hupkes, B. Rech, Thin Solid Films 442/1-2 (2003) 167.

[95] X.T. Hao, J. Ma, D.H. Zhang, Y.G. Yang, H.L. Ma, C.F. Cheng, X.D. Liu, Mater. Sci. Eng., B, Solid-State Mater. Adv. Technol. 90/1-2 (2002) 50.

[96] Y. Igasaki, H. Kanma, Appl. Surf. Sci. 169 (2001) 508.

[97] H.T. Cao, C. Sun, Z.L. Pei, A.Y. Wang, L.S. Wen, R.J. Hong, X. Jiang, J. Mater. Sci., Mater. Electron. 15/3 (2004) 169.

[98] E. Fortunato, V. Assuncao, A. Goncalves, A. Marques, H. Aguas, L. Pereira, I. Ferreira, P. Vilarinho, R. Martins, Thin Solid Films 451–52 (2004) 443.

[99] V. Assuncao, E. Fortunato, A. Marques, H. Aguas, I. Ferreira, M.E.V. Costa, R. Martins, Thin Solid Films 427/1-2 (2003) 401.

[100] T. Minami, T. Yamamoto, T. Miyata, Thin Solid Films 366/1-2 (2000) 63.

[101] A.S. Reddy, P.S. Reddy, S. Uthanna, G.M. Rao, J. Mater. Sci., Mater. Electron. 17/8 (2006) 615.

[102] R.E. Stauber, J.D. Perkins, P.A. Parilla, D.S. Ginley, Electrochem. Solid-State Lett. 2/12 (1999) 654.

[103] A.N. Banerjee, K.K. Chattopadhyay, J. Appl. Phys. 97/8 (2005) 084308.

[104] H. Hiramatsu, K. Ueda, H. Ohta, M. Orita, M. Hirano, H. Hosono, Thin Solid Films 411/1 (2002) 125.

[105] H. Hiramatsu, M. Orita, M. Hirano, K. Ueda, H. Hosono, J. Appl. Phys. 91/11 (2002) 9177.

[106] K. Ueda, S. Inoue, S. Hirose, H. Kawazoe, H. Hosono, Appl. Phys. Lett. 77/17 (2000) 2701.

[107] H. Sato, T. Minami, S. Takata, T. Yamada, Thin Solid Films 236/1-2 (1993) 27.

[108] T. Minami, K. Shimokawa, T. Miyata, J. Vac. Sci. Technol. A, Vac. Surf. Films 16/3 (1998) 1218.

[109] P.F. Carcia, R.S. McLean, M.H. Reilly, G. Nunes, Appl. Phys. Lett. 82/7 (2003) 1117.

[110] A.V. Singh, R.M. Mehra, A. Wakahara, A. Yoshida, J. Appl. Phys. 93/1 (2003) 396.

[111] I. Baia, M. Quintela, L. Mendes, P. Nunes, R. Martins, Thin Solid Films 337/1-2 (1999) 171.

[112] K. Ellmer, R. Cebulla, R. Wendt, Thin Solid Films 317/1-2 (1998) 413.

[113] Y. Hagiwara, T. Nakada, A. Kunioka, Sol. Energy Mater. Sol. Cells 67/1-4 (2001) 267.

[114] S. Christoulakis, M. Suchea, M. Katharakis, N. Katsarakis, E. Koudoumas, G. Kiriakidis, Rev. Adv. Mater. Sci. 10/4 (2005) 331.

[115] M. Grundmann, H. von Wenckstern, R. Pickenhain, T. Nobis, A. Rahm, M. Lorenz, Superlattices Microstruct. 38/4-6 (2005) 317.

[116] K. Matsubara, P. Fons, K. Iwata, A. Yamada, S. Niki, Thin Solid Films 422/1-2 (2002) 176.

[117] L. Dupont, C. Maugy, N. Naghavi, C. Guery, J.M. Tarascon, J. Solid State Chem. 158/2 (2001) 119.

[118] H. Izumi, T. Ishihara, H. Yoshioka, M. Motoyama, Thin Solid Films 411/1 (2002) 32.

[119] S.H. Kim, N.M. Park, T.Y. Kim, G.Y. Sung, Thin Solid Films 475/1-2 (2005) 262.

[120] J.B. Choi, J.H. Kim, K.A. Jeon, S.Y. Lee, Mater. Sci. Eng., B, Solid-State Mater. Adv. Technol. 102/1-3 (2003) 376.

[121] Y. Furubayashi, T. Hitosugi, Y. Yamamoto, Y. Hirose, G. Kinoda, K. Inaba, T. Shimada, T. Hasegawa, Thin Solid Films 496/1 (2006) 157.

[122] T. Hitosugi, Y. Furubayashi, A. Ueda, K. Itabashi, K. Inaba, Y. Hirose, G. Kinoda, Y. Yamamoto, T. Shimada, T. Hasegawa, Jpn. J. Appl. Phys., Part 2 Lett. Express Lett. 44/33–36 (2005) L1063.

[123] H. Agura, H. Okinaka, S. Hoki, T. Aoki, A. Suzuki, T. Matsushita, M. Okuda, Electr. Eng. Jpn. 151/2 (2005) 40.

[124] H. Agura, A. Suzuki, T. Matsushita, T. Aoki, M. Okuda, Thin Solid Films 445/2 (2003) 263.

[125] V. Bhosle, J. Narayan, J. Appl. Phys. 100/9 (2006) 093519.

[126] V. Bhosle, A. Tiwari, J. Narayan, J. Appl. Phys. 100/3 (2006) 033713.

[127] S.J. Henley, M.N.R. Ashfold, D. Cherns, Surf. Coat. Technol. 177 (2004) 271.

[128] W.J. Lee, C.R. Cho, K.M. Cho, S.Y. Jeong, J. Korean Phys. Soc. 47 (2005) S296.

[129] K. Matsubara, P. Fons, K. Iwata, A. Yamada, K. Sakurai, H. Tampo, S. Niki, Thin Solid Films 431 (2003) 369.

[130] K. Ramamoorthy, C. Sanjeeviraja, M. Jayachandran, K. Sankaranarayanan, V. Ganesan, P. Misra, L.M. Kukreja, Mater. Sci. Semicond. Process. 8/4 (2005) 555.

[131] R.K. Shukla, A. Srivastava, A. Srivastava, K.C. Dubey, J. Cryst. Growth 294/2 (2006) 427.

[132] A.V. Singh, R.M. Mehra, N. Buthrath, A. Wakahara, A. Yoshida, J. Appl. Phys. 90/11 (2001) 5661.

[133] U.S. Joshi, Y. Matsumoto, K. Itaka, M. Sumiya, H. Koinuma, Appl. Surf. Sci. 252/7 (2006) 2524.

[134] T. Minami, H. Tanaka, T. Shimakawa, T. Miyata, H. Sato, Jpn. J. Appl. Phys., Part 2 Lett. Express Lett. 43/7A (2004) L917.

[135] S. Sheng, G.J. Fang, C. Li, Z.Q. Chen, S. Ma, L.G. Fang, X.Z. Zhao, Semicond. Sci. Technol. 21/5 (2006) 586.

[136] H. Yanagi, S. Inoue, K. Ueda, H. Kawazoe, H. Hosono, N. Hamada, J. Appl. Phys. 88/7 (2000) 4159.

[137] V. Craciun, D. Craciun, X. Wang, T.J. Anderson, R.K. Singh, Thin Solid Films 453–54 (2004) 256.

[138] A. Suzuki, T. Matsushita, T. Aoki, A. Mori, M. Okuda, Thin Solid Films 411/1 (2002) 23.

[139] A. Suzuki, T. Matsushita, T. Aoki, Y. Yoneyama, M. Okuda, Jpn. J. Appl. Phys., Part 2- Lett. 40/4B (2001) L401.

[140] D.R. Sahu, J.L. Huang, Thin Solid Films 515/3 (2006) 876.

[141] K.L. Choy, Prog. Mater. Sci. 48/2 (2003) 57.

[142] J. Ni, H. Yan, A.C. Wang, Y. Yang, C.L. Stern, A.W. Metz, S. Jin, L. Wang, T.J. Marks, J.R. Ireland, C.R. Kannewurf, J. Am. Chem. Soc. 127/15 (2005) 5613.

[143] A.W. Metz, J.R. Ireland, J.G. Zheng, R. Lobo, Y. Yang, J. Ni, C.L. Stern, V.P. Dravid, N. Bontemps, C.R. Kannewurf, K.R. Poeppelmeier, T.J. Marks, J. Am. Chem. Soc. 126/27 (2004) 8477.

[144] A. Gulino, P. Dapporto, P. Rossi, I. Fragala, Chem. Mater. 14/12 (2002) 4955.

[145] L.C. Olsen, F.W. Addis, L. Huang, W.N. Shafarman, P. Eschbach, G.J. Exarhos, Proc. 28th IEEE PVSC, 2000, p. 458.

[146] X. Li, Y. Yan, A. Mason, T.A. Gessert, T.J. Coutts, Electrochem. Solid-State Lett. 4/9 (2001) C66.

[147] X. Li, D.L. Young, H. Moutinho, Y. Yan, C. Narayanswamy, T.A. Gessert, T.J. Coutts, Electrochem. Solid-State Lett. 4/6 (2001) C43.

[148] A.W. Metz, M.A. Lane, C.R. Kannewurf, K.R. Poeppelmeier, T.J. Marks, Chem. Vap. Depos. 10/6 (2004) 297.

[149] X. Li, T. Gessert, C. DeHart, T. Barnes, H. Moutinho, Y. Yan, D. Young, M. Young, J. Perkins, T.J. Coutts, A Comparison of Composite Transparent Conducting Oxides Based on the Binary Compounds CdO and SnO$_2$, NREL/CP-520-31017, 2001.

[150] J.P. Chatelon, C. Terrier, J.A. Roger, Semicond. Sci. Technol. 14/7 (1999) 642.

[151] D.C. Altamirano-Juarez, G. Torres-Delgado, R. Castanedo-Perez, O. Jimenez-Sandoval, J. Marquez-Marin, S. Jimenez-Sandoval, Superficies y Vacío, vol. 13, 2001, p. 66.

[152] G.J. Exarhos, S.K. Sharma, Thin Solid Films 270/1-2 (1995) 27.

[153] L.A. Chick, L.R. Pederson, G.D. Maupin, J.L. Bates, L.E. Thomas, G.J. Exarhos, Mater. Lett. 10/1-2 (1990) 6.

[154] L.R. Pederson, L.A. Chick, G.J. Exarhos, U.S. Pat. No. 4880772 (1989).

[155] T.P. Niesen, M.R. De Guire, J. Electroceram. 6/3 (2001) 169.

[156] T.P. Niesen, M.R. De Guire, Solid State Ion. 151/1-4 (2002) 61.

[157] B. Houng, Appl. Phys. Lett. 87/25 (2005) 251922.

[158] L. Wang, M.H. Yoon, G. Lu, Y. Yang, A. Facchetti, T.J. Marks, Nat. Mater. 5/11 (2006) 893.

[159] K. Domansky, A. Rose, W.H. Grover, G.J. Exarhos, Mater. Sci. Eng., B, Solid-State Mater. Adv. Technol. 76/2 (2000) 116.

[160] G.L. Messing, S.C. Zhang, G.V. Jayanthi, J. Am. Ceram. Soc. 76/11 (1993) 2707.

[161] X.D. Zhou, S.C. Zhang, W. Huebner, P.D. Ownby, H.C. Gu, J. Mater. Sci. 36/15 (2001) 3759.

[162] J.J. Prince, S. Ramamurthy, B. Subramanian, C. Sanjeeviraja, M. Jayachandran, J. Cryst. Growth 240/1-2 (2002) 142.

[163] P.K. Manoj, K.G. Gopchandran, P. Koshy, V.K. Vaidyan, B. Joseph, Opt. Mater. 28/12 (2006) 1405.

[164] D.J. Seo, S.H. Park, Physica, B 357/3-4 (2005) 420.

[165] S. Mirzapour, S.M. Rozati, M.G. Takwale, B.R. Marathe, V.G. Bhide, Mater. Res. Bull. 27/9 (1992) 1133.

[166] Y. Sawada, C. Kobayashi, S. Seki, H. Funakubo, Thin Solid Films 409/1 (2002) 46.

[167] Y. Sawada, Advanced Materials Processing Ii, vol. 437-4, Trans Tech Publications Ltd, Zurich-Uetikon, 2003, p. 23.

[168] M.M. Bagheri-Mohagheghi, M. Shokooh-Saremi, Thin Solid Films 441/1-2 (2003) 238.

[169] K.S. Shamala, L.C.S. Murthy, K.N. Rao, Bull. Mater. Sci. 27/3 (2004) 295.

[170] B. Thangaraju, Thin Solid Films 402/1-2 (2002) 71.

[171] P. Veluchamy, M. Tsuji, T. Nishio, T. Aramoto, H. Higuchi, S. Kumazawa, S. Shibutani, J. Nakajima, T. Arita, H. Ohyama, A. Hanafusa, T. Hibino, K. Omura, Sol. Energy Mater. Sol. Cells 67/1-4 (2001) 179.

[172] A. Gupta, D.K. Pandya, S.C. Kashyap, Jpn. J. Appl. Phys., Part 2 Lett. Express Lett. 43/12B (2004) L1592.

[173] K. Gurumurugan, D. Mangalaraj, S.K. Narayandass, C. Balasubramanian, Phys. Status Solidi, A Appl. Res. 143/1 (1994) 85.

[174] K. Gurumurugan, D. Mangalaraj, S.K. Narayandass, K. Sekar, C.P.G. Vallabhan, Semicond. Sci. Technol. 9/10 (1994) 1827.

[175] O. Vigil, L. Vaillant, F. Cruz, G. Santana, A. Morales-Acevedo, G. Contreras-Puente, Thin Solid Films 361 (2000) 53.

[176] J.H. Lee, S.Y. Lee, B.O. Park, Mater. Sci. Eng., B, Solid-State Mater. Adv. Technol. 127/2-3 (2006) 267.

[177] J.H. Lee, B.O. Park, Mater. Sci. Eng., B, Solid-State Mater. Adv. Technol. 106/3 (2004) 242.

[178] P. Pushparajah, A.K. Arof, S. Radhakrishna, J. Phys. D: Appl. Phys. 27/7 (1994) 1518.

[179] C. Gumus, O.M. Ozkendir, H. Kavak, Y. Ufuktepe, J. Optoelectron. Adv. Mater. 8/1 (2006) 299.

[180] A.F. Aktaruzzaman, G.L. Sharma, L.K. Malhotra, Thin Solid Films 198/1-2 (1991) 67.

[181] J.C. Manifacier, L. Szepessy, J.F. Bresse, M. Perotin, R. Stuck, Mater. Res. Bull. 14/1 (1979) 109.

[182] E. Elangovan, K. Ramamurthi, J. Optoelectron. Adv. Mater. 5/1 (2003) 45.

[183] K. Omura, P. Veluchamy, M. Tsuji, T. Nishio, M. Murozono, J. Electrochem. Soc. 146/6 (1999) 2113.

[184] G.C. Morris, A.E. McElnea, Appl. Surf. Sci. 92 (1996) 167.

[185] T.J. Coutts, D.L. Young, X.N. Li, MRS Bull. 25/8 (2000) 58.

[186] R. Cremer, D. Neuschutz, Surf. Coat. Technol. 146 (2001) 229.

[187] T. Kamiya, K. Nomura, H. Hosono, ECS 210th Meeting Abstract: Abstract, vol. 1598, 1996.

[188] J. Perkins, M.F.A.M. van Hest, C.W. Teplin, J.L. Alleman, M.S. Dabney, L.M. Gedvilas, B.M. Keyes, T.B., D.S. Ginley, M.P. Taylor, D.W. Readey, A.E. Delahoy, S. Guo, Optimization of Transparent Conducting Oxides (TCOs) for PV, NREL/CP-520-37420, 2005.

[189] H.M. Christen, S.D. Silliman, K.S. Harshavardhan, Rev. Sci. Instrum. 72/6 (2001) 2673.

[190] C. Kilic, A. Zunger, Phys. Rev. Lett. 88/9 (2002) 095501.

[191] O.N. Mryasov, A.J. Freeman, Phys. Rev., B 64/23 (2001) 233111.

[192] S. Narushima, M. Orita, M. Hirano, H. Hosono, Phys. Rev., B 66/3 (2002) 035203.

[193] E. Conwell, V.F. Weisskopf, Phys. Rev. 77/3 (1950) 388.

[194] H. Brooks, Phys. Rev. 83/4 (1951) 879.

[195] T. Makino, Y. Segawa, A. Tsukazaki, A. Ohtomo, M. Kawasaki, Appl. Phys. Lett. 87/2 (2005) 022101.

[196] D.C. Look, J.W. Hemsky, J.R. Sizelove, Phys. Rev. Lett. 82/12 (1999) 2552.

[197] J.R. Lowney, H.S. Bennett, J. Appl. Phys. 69/10 (1991) 7102.

[198] G. Masetti, M. Severi, S. Solmi, IEEE Trans. Electron Devices 30/7 (1983) 764.

[199] A. Tsukazaki, A. Ohtomo, M. Kawasaki, Appl. Phys. Lett. 88/15 (2006) 152106.

[200] Y.Z. Chiou, K.W. Lin, J. Electrochem. Soc. 153/2 (2006) G141.

[201] Q. Wan, E.N. Dattoli, W.Y. Fung, W. Guo, Y.B. Chen, X.Q. Pan, W. Lu, Nano Lett. 6/12 (2006) 2909.

[202] C. Agashe, O. Kluth, J. Hupkes, U. Zastrow, B. Rech, M. Wuttig, J. Appl. Phys. 95/4 (2004) 1911.

[203] S.H. Keshmiri, M. Rezaee-Roknabadi, S. Ashok, Thin Solid Films 413/1-2 (2002) 167.

[204] I.A. Rauf, J. Appl. Phys. 79/8 (1996) 4057.

[205] D.H. Zhang, H.L. Ma, Appl. Phys., A Mater. Sci. Process. 62/5 (1996) 487.

[206] H. Tanaka, K. Ihara, T. Miyata, H. Sato, T. Minami, J. Vac. Sci. Technol. A, Vac. Surf. Films 22/4 (2004) 1757.

[207] A. Wang, J.R. Babcock, N.L. Edleman, A.W. Metz, M.A. Lane, R. Asahi, V.P. Dravid, C.R. Kannewurf, A.J. Freeman, T.J. Marks, Proc. Natl. Acad. Sci. U. S. A. 98/13 (2001) 7113.

[208] M. Yan, M. Lane, C.R. Kannewurf, R.P.H. Chang, Appl. Phys. Lett. 78/16 (2001) 2342.

[209] S. Jin, Y. Yang, J.E. Medvedeva, J.R. Ireland, A.W. Metz, J. Ni, C.R. Kannewurf, A.J. Freeman, T.J. Marks, J. Am. Chem. Soc. 126/42 (2004) 13787.

[210] G.J. Exarhos, A. Rose, L.Q. Wang, C.F. Windisch, J. Vac. Sci. Technol. A, Vac. Surf. Films 16/3 (1998) 1926.

[211] G.J. Exarhos, A. Rose, C.F. Windisch, Thin Solid Films 308 (1997) 56.

[212] C. Kilic, A. Zunger, Appl. Phys. Lett. 81/1 (2002) 73.

[213] C.G. Van de Walle, Phys. Rev. Lett. 85/5 (2000) 1012.

[214] S.J. Jokela, M.D. McCluskey, Phys. Rev., B 72/11 (2005) 113201.

[215] M.D. McCluskey, S.J. Jokela, K.K. Zhuravlev, P.J. Simpson, K.G. Lynn, Appl. Phys. Lett. 81/20 (2002) 3807.

[216] L.Y. Chen, W.H. Chen, J.J. Wang, F.C.N. Hong, Y.K. Su, Appl. Phys. Lett. 85/23 (2004) 5628.

[217] F. Ruske, V. Sittinger, W. Werner, B. Szyszka, K.U. van Osten, K. Dietrich, R. Rix, Surf. Coat. Technol. 200/1-4 (2005) 236.

[218] Y.M. Strzhemechny, J. Nemergut, P.E. Smith, J. Bae, D.C. Look, L.J. Brillson, J. Appl. Phys. 94/7 (2003) 4256.

[219] Y.M. Strzhemechny, H.L. Mosbacker, S.H. Goss, D.C. Look, D.C. Reynolds, C.W. Litton, N.Y. Garces, N.C. Giles, L.E. Halliburton, S. Niki, L.J. Brillson, J. Electron. Mater. 34/4 (2005) 399.

[220] M. Li, J. Zhai, H. Liu, Y.L. Song, L. Jiang, D.B. Zhu, J. Phys. Chem., B 107/37 (2003) 9954.

[221] L.Q. Wang, G.J. Exarhos, C.F. Windisch, C. Yao, L.R. Pederson, X.-D. Zhou, Appl. Phys. Lett. (In press).

[222] P.V. Sushko, A.L. Shluger, K. Hayashi, M. Hirano, H. Hosono, Phys. Rev. Lett. 91/12 (2003) 126401.

[223] Z.Y. Li, J.L. Yang, J.G. Hou, Q.S. Zhu, Angew. Chem., Int. Ed. Engl. 43/47 (2004) 6479.

[224] J.E. Medvedeva, A.J. Freeman, Appl. Phys. Lett. 85/6 (2004) 955.

[225] G. Dolling, M. Wegener, C.M. Soukoulis, S. Linden, Opt. Lett. 32/1 (2007) 53.

[226] I.R. Hooper, T.W. Preist, J.R. Sambles, Phys. Rev. Lett. 97/5 (2006) 053902.

[227] S.W. Chen, C.H. Koo, H.E. Huang, C.H. Chen, Mater. Trans. 46/11 (2005) 2536.

[228] T.W. Ebbesen, H.J. Lezec, H.F. Ghaemi, T. Thio, P.A. Wolff, Nature 391/6668 (1998) 667.

[229] J.W. Lee, M.A. Seo, J.Y. Sohn, Y.H. Ahn, D.S. Kim, S.C. Jeoung, C. Lienau, Q.H. Park, Opt. Express 13/26 (2005) 10681.

[230] A. Rose, G.J. Exarhos, Thin Solid Films 308 (1997) 42.